

ORIGINAL ARTICLE

# Disrupted Timing of MET Signaling Derails the Developmental Maturation of Cortical Circuits and Leads to Altered Behavior in Mice

Xiaokuang Ma<sup>1</sup>, Jing Wei<sup>1</sup>, Yuehua Cui<sup>1</sup>, Baomei Xia<sup>1</sup>, Le Zhang<sup>1</sup>, Antoine Nehme<sup>1</sup>, Yi Zuo<sup>2</sup>, Deveroux Ferguson<sup>1</sup>, Pat Levitt<sup>3</sup> and Shenfeng Qiu<sup>1</sup>

<sup>1</sup>Basic Medical Sciences, University of Arizona College of Medicine-Phoenix, Phoenix, AZ 85004, USA,

<sup>2</sup>Department of Molecular, Cellular and Developmental Neurobiology, University of California at Santa Cruz, Santa Cruz, CA 95064, USA and <sup>3</sup>Program in Developmental Neuroscience and Developmental Neurogenetics, The Saban Research Institute and Department of Pediatrics, Children's Hospital Los Angeles, Keck School of Medicine, University of Southern California, Los Angeles, CA 90027, USA

Address correspondence to Shenfeng Qiu, Basic Medical Sciences, University of Arizona College of Medicine-Phoenix, 425 N. 5th ST, Phoenix, AZ 85004, USA. Email: [sqiu@email.arizona.edu](mailto:sqiu@email.arizona.edu)

## Abstract

The molecular regulation of the temporal dynamics of circuit maturation is a key contributor to the emergence of normal structure–function relations. Developmental control of cortical MET receptor tyrosine kinase, expressed early postnatally in subpopulations of excitatory neurons, has a pronounced impact on the timing of glutamatergic synapse maturation and critical period plasticity. Here, we show that using a controllable overexpression (cto-Met) transgenic mouse, extending the duration of MET signaling after endogenous *Met* is switched off leads to altered molecular constitution of synaptic proteins, persistent activation of small GTPases Cdc42 and Rac1, and sustained inhibitory phosphorylation of cofilin. These molecular changes are accompanied by an increase in the density of immature dendritic spines, impaired cortical circuit maturation of prefrontal cortex layer 5 projection neurons, and altered laminar excitatory connectivity. Two photon in vivo imaging of dendritic spines reveals that cto-Met enhances de novo spine formation while inhibiting spine elimination. Extending MET signaling for two weeks in developing cortical circuits leads to pronounced repetitive activity and impaired social interactions in adult mice. Collectively, our data revealed that temporally controlled MET signaling as a critical mechanism for controlling cortical circuit development and emergence of normal behavior.

**Key words:** autism, circuit connectivity, cortical circuits, molecular mechanisms, neurodevelopmental disorders, plasticity, synapses

## Introduction

Formation of proper synaptic connectivity during cortical circuit development that leads to normal functions requires regulated neuronal growth, balanced excitatory and inhibitory synapse production and elimination, and properly timed maturation and plasticity (Tau and Peterson 2010; Jabaudon 2017; Reh et al. 2020). Molecular signaling mediated through receptor tyrosine kinases profoundly shapes these processes (Lemmon and Schlessinger 2010; Park and Poo 2013). Disruption of these processes is a hallmark pathology of many neurodevelopmental and neuropsychiatric disorders, including autism spectrum disorder (ASD) (Levitt and Campbell 2009; Penzes et al. 2011; Guang et al. 2018; Bagni and Zukin 2019; Sullivan and Geschwind 2019).

The human *MET* gene, which encodes a receptor tyrosine kinase, was identified initially in a family-based genetic study as a high-confidence ASD risk gene (Campbell et al. 2006), based on the rs1858830 “C” allele in the proximal promoter. The allele also reduces gene transcription by ~50%. While subsequent large-scale studies indicate that the receptor is not causal for ASD (Campbell et al. 2006; Lambert et al. 2014; Eagleson et al. 2017), *MET* expression is reduced by approximately 50% in postmortem neocortex from ASD patients (Campbell et al. 2007; Aldinger et al. 2015) and is nearly absent in Rett syndrome (Aldinger et al. 2015; Aldinger et al. 2020). Remarkably, while not an ASD causal gene, human functional neuroimaging studies show that the “C” allele is highly correlated with altered cortical functional connectivity (Rudie et al. 2012). Numerous neurodevelopmental studies have demonstrated that *MET* mediates pleiotropic signaling in the developing neocortex and hippocampus, by engaging multiple intracellular molecular pathways that collectively regulate excitatory pyramidal neuron dendritic arborization, spine morphology, excitatory synapse maturation, and cortical plasticity (Qiu et al. 2014; Eagleson et al. 2016; Peng et al. 2016; Xie et al. 2016; Eagleson et al. 2017).

In primate and mouse neocortices, *MET* is primarily expressed in excitatory neurons during late prenatal and early postnatal development but is precipitously downregulated prior to circuit maturation (Judson et al. 2009; Judson et al. 2011; Eagleson et al. 2016). This early expression coincides with periods of heightened structural changes including neurite growth and spine morphogenesis but precedes the milestones of functional synapse maturation and experience-dependent refinement of connectivity (Hensch 2005; Fox et al. 2010; Kast and Levitt 2019). The conserved temporal feature of regulated *MET* signaling, irrespective of species, cortical regions, and cell types (Judson et al. 2009; Judson et al. 2011), is indicative of conserved developmental functions. We hypothesized that timely termination of *MET* signaling is a critical molecular shift that is necessary for subsequent cortical circuit development and typical behaviors. Utilizing a novel controllable *Met* overexpression mouse line (cto-*Met*), we have recently shown that extending *MET* signaling in the visual cortex alters dendritic and spine structure, synaptic activity, and the timing of critical period plasticity (Chen et al. 2020). Yet there remains a limited understanding of the implications of regulated or disrupted timing of developmental signaling onset and offset.

Here, we report that extending *MET* signaling duration results in profound changes in morphology of prefrontal cortex projection neurons, synaptic function, and intracortical circuit connectivity. These aberrant *MET* signaling-induced changes were accompanied by increased activation of small GTPases

Cdc42 and Rac1, persistent inhibition of cofilin, increased *de novo* dendritic spine production, and reduced elimination during the postnatal period of developing cortical circuits. Interestingly, extending the duration of *MET* signaling for just two weeks leads to persistent behavioral disturbances in adult mice. Our data suggest that temporally controlled *MET* signaling serves as a novel mechanism for controlling the maturation timing and functional readout of cortical circuits.

## Materials and Methods

### Animals

The development of the controllable transgenic *Met* mouse line for sustained/overexpression of *MET* protein was reported previously (Chen et al. 2020). Briefly, a *Met* cDNA (NM\_008591) construct was tagged on the C-terminus with Myc-FLAG epitope and cloned into the pTRE-Tight vector (Clontech) downstream to a tetracycline response element (TRE) in a “tet-off” configuration (Gossen and Bujard 1992). The transgenic *MET* line (TRE-*MET*) was crossed to CaMKII-*tTA* mice (Mayford et al. 1996) to obtain the controllable transgenic overexpression mice for *MET* (cto-*Met*) in dorsal pallial excitatory neurons. This allows artificial control of the *Met* transgene expression through doxycycline-containing chow (DOX, 625 mg/kg, Harlan Laboratories); cto-*Met* is suppressed by DOX chow but can be turned on after switching to DOX-free chow (Chen et al. 2020). cto-*MET* mice have a normal gestational period and no statistically significant difference in size as same-sex littermate controls.

The forebrain-specific conditional mutant mice (cKO, *Met<sup>fx/fx</sup>; emx1<sup>Cre</sup>*) was described previously (Judson et al. 2009; Qiu et al. 2014), by breeding homozygous female *Met<sup>fx/fx</sup>* mice to hemizygote *Met<sup>fx/+</sup>* male mice with an *emx1<sup>Cre</sup>* knock-in allele (Gorski et al. 2002). Mutant mice were genotyped by polymerase chain reaction (PCR) as described previously (Judson et al. 2009; Judson et al. 2011). Mice IDs and data were coded so that the experimenters were blinded to genotypes and grouping. An approximately equal number of male and female mice were used in this study. All experimental procedures were approved by the Institutional Animal Care and Use Committee of the University of Arizona.

### Western Blot and Biochemical Analyses

Microdissected prefrontal (pre- and infralimbic) and hippocampus (CA1) tissues were homogenized in cold NP40 cell lysis buffer (FNN0021, Fisher Scientific) supplemented with proteinase inhibitor cocktail (PIC, 1:50, Sigma P8340) and 1 mM phenylmethylsulfonyl fluoride (PMSF). To obtain synaptosome fractions, PFC tissues were manually homogenized in cold buffer (containing 4 mM HEPES, 320 mM sucrose, and 1:50 PIC). The homogenates were centrifuged at 1500 × *g* for 10 min. The supernatant was collected and further centrifuged at 16000 × *g* for 20 min to yield a crude synaptosome pellet. Protein content for the whole tissue homogenate and synaptosome was quantified using a micro-BCA assay. Samples were mixed with equal amount of 2 × Laemmli loading buffer and boiled for 5 min and then separated by 4–15% gradient SDS polyacrylamide gels (Bio-Rad). The proteins were transferred to PVDF membranes (Immobilon-P, Millipore), blocked with 5% nonfat dry milk, and incubated with primary antibodies overnight at 4 °C, followed by incubation with HRP-conjugated secondary antibodies

(Promega) for 2 h at RT. In some experiments in which both phosphorylated and total proteins were to be probed, a stripping buffer was used to remove the membrane signal to allow repeated detection with a different antibody. To measure the GTP-bound, activated Rac1/Cdc42, we used a Rac1/Cdc42 activation assay kit (Millipore, 17–441). The kit utilizes a glutathione-S-transferase fused with the p21-binding domain of p21-activated protein kinase PAK1. The fusion protein only binds to GTP-bound, activated form of Cdc42 or Rac1. The final dilution of antibodies was between 1:1000 and 1:2000. Protein signals were developed using chemiluminescence (SignalFire, Cell Signaling Technology) and captured on ECL Hyperfilm (Amersham).

The following antibodies were used: from Santa Cruz Biotechnology, anti-MET (sc-8057); from Millipore/Chemicon, rabbit anti-GluA1 (AB5849); from Cell Signaling Technology, rabbit anti-GluN2A (#4205), rabbit anti-GluN2B (#14544), rabbit anti-GAPDH (#5174), rabbit anti-cofilin (#5175), rabbit anti-PAK1 (#2602), rabbit anti-p-PAK1/2 (T423/402, #2601), rabbit anti-LIMK1 (#3842), rabbit anti-phospho-cofilin (Ser3) (#3313), rabbit anti-Myc (71D10) (#2278). The final dilution of antibodies was between 1:1000 and 1:2000. The optical density of immunoreactive bands was quantified by densitometry using FIJI/ImageJ.

### Retrobeads Labeling of PFC Corticostriatal Neurons

To enable comparison of the same projection neuron type between groups, fluorescent latex microspheres (“retrobeads”, Lumafuor) were used to label contralaterally projecting corticostriatal (CST) neurons in prefrontal cortex (Qiu et al. 2011). Mice were anesthetized and stereotactically injected with 50 nL red retrobeads into the left dorsolateral striatum (coordinates: relative to bregma: 0.0 mm posterior, 2.0 mm lateral, 2.5 mm ventral). The injection glass pipette was held in place for 10 min before withdrawing slowly from the injection site. In all cases, animals received injections >24 h before being sacrificed for brain slice preparation.

### Whole-Cell Patch-Clamp Recording in Brain Slices

Mice were euthanized with 3–5% isoflurane. To enhance brain slice viability, intracardiac perfusion was performed using ice-cold choline solution (contains in mM: 110 choline chloride, 25 NaHCO<sub>3</sub>, 2.5 KCl, 1.25 NaH<sub>2</sub>PO<sub>4</sub>, 0.5 CaCl<sub>2</sub>, 7 MgSO<sub>4</sub>, 11.6 sodium ascorbate, 25 D-glucose, and 3.1 sodium pyruvate, saturated with 95% O<sub>2</sub>/5% CO<sub>2</sub>). Mice were decapitated and brains were quickly dissected. Parasagittal prefrontal slices (300  $\mu$ m thick) at the anterior frontal level were made in ice-cold choline solution using a vibratome (VT-1200S, Leica). Slices were immersed in artificial cerebrospinal fluid (ACSF, contains in mM: 126 NaCl, 2.5 KCl, 26 NaHCO<sub>3</sub>, 2 CaCl<sub>2</sub>, 2 MgCl<sub>2</sub>, 1.25 NaH<sub>2</sub>PO<sub>4</sub>, and 10 d-glucose; saturated with 95% O<sub>2</sub>/5% CO<sub>2</sub>) for 30 min at 35 °C and then maintained at RT (24 °C) until recording.

Slices were visualized under a 4 $\times$  objective to allow identification of PFC laminar landmarks. L5 neurons with soma at least 50  $\mu$ m below the slice surface were selected for whole-cell recordings under a 60 $\times$  water immersion objective (Olympus, NA = 0.9). Spontaneous neuronal responses were amplified using a MultiClamp 700B amplifier, low-pass filtered at 1 kHz (current signals) or 10 kHz (voltage signals) and digitized at 20 kHz using a Digidata 1440A interface (Molecular Devices, San Jose, CA). Miniature excitatory postsynaptic currents (mEPSCs)

were recorded from beads+ CSt L5 neurons at  $V_{\text{hold}} = -70$  mV, in the presence of TTX (1  $\mu$ M) and D-AP5 (50  $\mu$ M). The electrode internal solution contained (in mM): 130 K-gluconate, 4 KCl, 2 NaCl, 10 HEPES, 4 ATP-Mg, 0.3 GTP-Na, 1 EGTA, and 14 phosphocreatine (pH 7.2, 295 mOsm). Inhibitory postsynaptic currents (mIPSCs) were measured at  $V_{\text{hold}} = -70$  mV with an internal solution that contains symmetrical [Cl<sup>-</sup>] and with CNQX (10  $\mu$ M) and TTX (1  $\mu$ M) added to the perfusate. The electrode internal solution for mIPSC recordings contained (in mM): 125 KCl, 2.8 NaCl, 2 MgCl<sub>2</sub>, 2 Mg<sup>2+</sup>-ATP, 0.3 Na<sub>3</sub>GTP, 10 HEPES, 1 EGTA, and 10 phosphocreatine (pH 7.25, ~300 mOsm). To record stimulus-evoked L2/3 > L5 synaptic responses, evoked monosynaptic responses were obtained, while L5 CS pyramidal neurons were voltage clamped at  $-70$  mV (AMPA-mediated synaptic currents) or +40 mV (AMPA+NMDAR), with a Cs<sup>+</sup>-based internal solution (contains in mM, 125 Cs-gluconate, 5 TEA-Cl, 10 HEPES, 2.5 CsCl, 8 NaCl, 5 QX314-HCl, 4 Mg<sup>2+</sup>-ATP, 0.3 Na<sub>3</sub>GTP, 1 EGTA, and 10 phosphocreatine, pH 7.25). A bipolar stimulating electrode (FHC) was placed in L23 of the PFC, and a stimulus isolator (Iso-flex, A.M.P.I.) was used to deliver a bipolar electrical stimulus.

### Laser Scanning Photostimulation for Cortical Circuit Mapping

Laser-scanning photostimulation (LSPS) mapping was performed as described previously (Suter et al. 2010; Qiu et al. 2011). Mice were sacrificed at P35–40. PFC slices were transferred to the recording chamber of a custom-built LSPS rig and were perfused in a modified ACSF that contains 0.2 mM MNI-caged glutamate (Tocris), 4 mM CaCl<sub>2</sub>, 4 mM MgCl<sub>2</sub>, and 5  $\mu$ M CPP (Tocris). Beads+ L5 CST neurons were patched clamped with a K-gluconate internal solution (see above). LSPS mapping was performed at 24 °C. Neuronal membrane properties were measured by a series of 5 mV hyperpolarizing voltage steps. Intrinsic properties were measured in current-clamp mode immediately before mapping, by presenting families of 1-s current steps (100–500 pA in 50 pA increments). Frequency–current relationships were first calculated based on the numbers of APs per current step. LSPS/glutamate uncaging was performed with a 4 $\times$  objective lens (NA 0.16; Olympus) and 20 mW, 1-ms UV laser (355 nm; DPSS Lasers) pulses. Digital images were registered using a CCD camera (Retiga 2000 DC, QImaging). A 16  $\times$  16 stimulation grids with 100- $\mu$ m spacing were registered onto the slice images. Electrophysiological signals were amplified with a MultiClamp 700B amplifier and acquired using BNC-6259 data acquisition boards (National Instruments). We used Ephus software (Suter et al. 2010) to control data acquisition and MATLAB routines for offline analysis.

### Neuronal Morphology

Neurolucida (MicroBrightField) and Imaris (V8.02, Bitplane) were used to reconstruct dendritic arbors and spines, respectively, of L5 neurons. Beads+ CSt neurons in live slices were filled with 0.25% biocytin using a patch-clamp electrode. Neurons were injected with 500 pA current for 10 min to facilitate diffusion of biocytin. The slices were then fixed in 4% PFA overnight, blocked in 1% BSA in PBS, permeabilized with 0.2% Triton X-100 in 0.01 M PBS, and incubated with avidin-alexa 488 for 24 h to reveal neuronal morphology.

Dendritic arbors of L5 CST neurons were traced using Neurolucida and were registered in three dimensions. Sholl analysis

(Sholl 1953) was performed to quantify dendritic arbor, dendritic length, and number of intersections using NeuroLucida Explorer. Between one and four cells were reconstructed per slice, and at least five mice per group were included for analyses. To quantify dendritic spine morphology, confocal Z-stack images of spines were collected from secondary apical dendritic branches that are 200–450  $\mu\text{m}$  from soma. Z-stacks ( $512 \times 512$  pixels,  $Z = 0.2 \mu\text{m}$ ) were collected with a  $63\times$  objectives (Zeiss Plan APOchromat, NA 1.4), using a  $4\times$  digital zoom. Imaris software was used to reconstruct the 3D spine images. The spines were further categorized as “filopodia,” “mushroom,” “stubby,” and “long thin” subtypes based on predefined features (Imaris MATLAB module), as reported previously (Peng et al. 2016).

## Two-Photon Dendritic Spine Imaging

Cto-Met mice were crossed to the Thy1-GFP line (Feng et al. 2000), and mutant mice (TRE-Met:TA:Thy1-GFP) were used for imaging. Control mice were littermates that did not contain the TRE-Met transgene. Mice were imaged longitudinally, first at P25 and then P32. Mice initially underwent a thinned skull surgery, similar to that described previously (Grutzendler et al. 2002; Fu et al. 2012; Ma et al. 2020). The skull over primary visual cortex (V1) was exposed based on the anatomically defined coordinates (Stephany et al. 2014). A high-speed drill (Osada) was used to reduce the skull thickness by  $\sim 50\%$ , while cooled sterile saline was applied to the skull intermittently to mitigate mechanical or excessive heat damage to the dendritic segments. A micro-dental blade was used to gently reduce the skull thickness to  $\sim 30\text{--}40 \mu\text{m}$ . We fixed a plastic liquid retention ring to aid the imaging using the water immersion objective. Mouse head was mounted on a customized small stereotaxic equipment connected to a custom-built miniaturized isoflurane mask, which allows free adjustment of head angles. Anesthesia during imaging was maintained by  $1\text{--}1.5\%$  isoflurane while mouse body temperature was maintained by a heating pad (Fine Science Tools). Mice were placed under a two-photon microscope (Olympus FV-MPS, “Apollo” system) and imaged with a  $25\times$  water immersion objective (NA 1.05, Olympus). A two-photon laser (Mai Tai DeepSee,  $690\text{--}1300 \text{ nm}$ , Spectra-Physics) was tuned to  $920 \text{ nm}$ , and  $<50 \text{ mW}$  laser power was pumped during imaging to reduce phototoxicity and bleaching.

Upon identifying a spiny L5 neuron dendritic segment, we first registered its location by taking a full field of view image that was centered on the spiny segment. Blood vessels served as the landmark to relocate this dendritic segment during the second imaging session. For each segment, a region of interest (ROI) centered on the dendritic segment was outlined, and a Z-stack of images was acquired using the galvanometer scanner with a digital zoom  $4.0\times$  and a step size of  $0.5 \mu\text{m}$ . The imaging depth was  $\sim 150\text{--}300 \mu\text{m}$  from the pia surface. To quantify spine dynamics during the 1-week period, the first imaging session was conducted right after preparation of thinned skull at P25. After the first imaging session, the scalp was closed and the mouse was returned to the cage. The thinned skull was reconditioned for the second imaging session at P32.

To analyze spine dynamics, FIJI/ImageJ was used to open the Z-stack images collected at both imaging sessions. Single image slices that were severely distorted by respiratory motion artifacts were discarded. The smaller motion artifacts for the rest of images were corrected using moco plugin (Dubbs et al. 2016).

A two-dimensional MIP projection image containing dendritic segments of interest was used to quantify spines. Any pixels that were not directly connected to the dendritic segment of interest (i.e., from other dendrites or coursing axons) were masked using Adobe Photoshop (Adobe systems). Because prolonged imaging may deteriorate the spines and lead to dendritic blebbing, we limited data collection to 1–3 segments from each mouse. Dendritic spines were defined as protrusions with a length that is at least  $50\%$  thickness of the adjoining dendritic shaft and were further verified by browsing through the Z-stacks. Spine formation and elimination rates across the 1-week period were calculated at each age after spines were manually identified and were normalized to the length of the segment. The total number of dendritic segments used to calculate spine formation/elimination rate was pooled from at least seven animals (male and female) of each genotype.

## Behavioral Analyses

### Open field test

Open field test (OF) was used to assess basal locomotor activity and behavioral reactivity to a novel environment. Mice were placed in an open field enclosure ( $45 \times 45 \text{ cm}^2$ ) and habituated for 10 min. A video-tracking system (EthoVision XT, Noldus Technologies, Leesburg, VA) was adopted to record activity for 10 min after habituation. Total distance and percent of time spent in the center of arena ( $22.5 \times 22.5 \text{ cm}^2$ ) were quantified.

### Elevated plus maze test

The elevated plus maze (EPM) test was used to evaluate anxiety-like behavior in mice by using their innate preference for dark and enclosed spaces. The EPM apparatus was elevated four feet from the ground and consisted of four runways ( $9 \text{ in} \times 2.5 \text{ in}$  rectangle) arranged perpendicularly, two of which were enclosed with 5-inch high walls (close arm) and two of which were open (open arm). The amount of time spent in the open arms and number of open arm entry were used as measurements of anxiety-like behavior. Activity was recorded by the EthoVision video-tracking system during the 5-min session.

### Repetitive Behaviors

During the morning in reduced ambient red light, mice in their home cages (containing fresh bedding) were monitored during a 30-min period for repetitive behaviors, including digging, jumping, and grooming. Digging was defined as the coordinated use of two fore limbs or hind legs to move out bedding materials. Jumping was defined as hind leg rearing at the corner/side of the cage, with jumps so that the two hind legs are simultaneously off the ground. Grooming was defined as licking body parts, or repeated stroking/scratching of the head, face, or body with the two forelimbs. For the marble-burying task, the test cage bottom was covered with  $\sim 5 \text{ cm}$  deep layer of bedding. A mouse was habituated to the cage for 10 min and then returned to the home cage. Twenty 15-mm-diameter glass marbles were placed on top of the bedding of the test cage in a  $4 \times 5$  arrangement. The mouse was returned to the test cage and the number of marbles buried ( $\geq 50\%$  of marble surface covered by bedding material) in 20 min was recorded.

### Three-Chamber Social Interaction Test

The three-chamber social interaction test (Silverman et al. 2010; Won et al. 2012; Rein et al. 2020) was used to assess sociability



and social novelty. The assay consisted of three phases. Animals were habituated in the three-chamber apparatus for 10 min on each of two days before testing. During phase 1 on the test day, a small wire cup that contained an oval-shaped object made from black foil was placed in left and right side of the apparatus. The mouse was placed in the center area and was allowed to explore the environment freely for 10 min. During phase 2, the mouse was gently guided to the center chamber and two side entrances from the center chamber were blocked. An inanimate object (nonsocial, NS) and an unfamiliar mouse (Soc1) were placed in different wire cups. The two entrances were then opened to allow the mouse to explore both arms freely for 10 min. In phase 3, the test mouse was gently guided to the center chamber. The two wire cups now each contained a novel stranger (Soc2) and the now-familiar mouse (Soc1). The test mouse was again allowed to explore and interact with both mice for 10 min. Social interaction was defined as each instance in which test mouse sniffed the objects/strangers, or oriented its nose toward and moved into the interaction zone (within 5 cm) of the wired cups. EthoVision XT 14.0 was used to measure time spent in each chamber and visualize the movement tracks and speed. We used the social preference index (SPI) in addition to time spent in each chamber, which is defined by the numerical difference between times spent exploring the test targets divided by total time spent exploring both targets.

#### Statistical Analyses

Data were processed using Image J, Microsoft Excel, MATLAB, GraphPad Prism 8.0, and Adobe Creative Cloud. Quantitative results were expressed as mean  $\pm$  s.e.m. Sex as a biological variable was addressed by first analyzing sex-disaggregated data and visualized separately on the graph where applicable. In all analyses, we did not observe a significant effect of sex, as such data from male and female were pooled for analysis. Shapiro-Wilk test and F test were used to test normality and equal variance. For normally distributed and equal variance data, Student t test or one-way/two-way analysis of variations (with optional post hoc Sidak's multiple comparison test/MCT) was used. For nonnormally distributed data, nonparametric Mann-Whitney U tests were performed. Potential data outliers (at least three standard deviations from the mean) were excluded from analysis. For dendritic arborization/Sholl analysis, a two-way ANOVA was used to assess group effects. Kolmogorov-Smirnov (K-S) test was employed to compare cumulative distribution of mEPSC/mIPSC amplitudes.  $P < 0.05$  was considered statistically significant for all tests.

## Results

### Temporal Control of MET Signaling in Cortical Circuits through Transgene Overexpression

We have previously shown that MET signaling in developing cortical circuits is under tight temporal regulation (Eagleson et al. 2016; Chen et al. 2020). Although there exists a regional and cell type specificity in the temporal regulation, in general, MET expression is strongest during the first two to three weeks in multiple cortical regions including the prefrontal cortex (PFC), hippocampus (HPC), and primary visual cortex (VC). Invariably, compared with expression levels during the first postnatal week, MET protein and signaling is precipitously downregulated by postnatal day (PD) 21 in all cortical regions (Chen et al. 2020).

In this study, to ascertain the functional significance of the signaling downregulation, we used a controllable Met transgenic mouse line (TRE-MET) (Chen et al. 2020) (see Materials and Methods) crossed to the CaMKII-tTA line (Mayford et al. 1996) (Fig. 1A) and focused on the effects of MET overexpression (OE) on PFC neuron structure and function. In the TRE-MET mouse line, MET expression is driven by the tetracycline response element (TRE) promoter, which does not lead to Met transgene expression in the absence of tTA (Fig. 1B). The double transgenic TRE-MET:tTA offspring that achieves MET OE is hereafter referred as controllable transgenic overexpression (cto-MET). Cto-MET allows exquisite temporal control of MET expression; Met transgene expression in cto-MET PFC can be completely suppressed by feeding the DOX-containing chow to the dam/litter from birth (detected by transgene Myc tag—Fig. 1B) at P21. In contrast, removal of DOX at P14 leads to long-lasting Met transgene expression when detected at 7 days and 6 weeks later (Fig. 1B).

In the P25–28 cto-MET PFC, while continued DOX led to cto-MET suppression and minimum endogenous MET signaling (Fig. 1C. Measured by pY1234/1235,  $n = 4$ ), removal of DOX at P14 resulted in dramatically increased pY1234/1235 in PFC tissue and to a lesser degree in the hippocampus CA1 tissue (Fig. 1C). As expected, cto-MET led to a marked increase of total MET protein. These data demonstrate that cto-MET signaling can be temporally controlled precisely by DOX.

### Extending MET Signaling in Cortical Circuits Alters Synaptic Proteins and Signaling Pathways Implicated in Spine Dynamics

We have previously found that in the developing VC, cto-MET led to increased activation of small GTPases Cdc42 and Rac1 (Chen et al. 2020). We asked whether this signaling is a general mechanism and also operates in developing PFC circuits. Probing P22–25 PFC tissues from cto-MET and its nontransgenic littermate controls revealed that cto-MET also resulted in significantly increased Cdc42 and Rac1 activation (Fig. 2A,  $P = 0.0029$  for Cdc42,  $P = 0.007$  for Rac1,  $n = 4$ ; quantification in Supplementary Fig. 1). Because Cdc42 and Rac1 are coupled to dendritic spine morphogenesis and actin dynamics through the actin depolymerizing factor cofilin (Arber et al. 1998; Yang et al. 1998; Sarmiere and Bamburg 2004; Pontrello et al. 2012; Bosch et al. 2014), we further probed levels of cofilin phosphorylation (p-Ser3) (Moriyama et al. 1996). We found that cto-MET led to a significant increase in p-Ser3 levels in both PFC and HPC tissues, without altering the total levels of cofilin protein (Fig. 2A, Supplementary Fig. 1,  $P = 0.011$  for PFC,  $P = 0.008$  for HPC,  $n = 4$ ).

To further test how cto-MET may affect the levels of PFC synaptic proteins related to synaptogenesis and synaptic function, we conducted western blot to quantify select synaptic proteins involved in synaptic transmission and maturation (Fig. 2B, Supplementary Fig. 1). In P22–25 PFC tissue lysates, cto-MET led to increased total levels of MET ( $P = 0.012$ ,  $n = 4$ ), p-LIMK1 (T508) ( $P = 0.011$ ,  $n = 4$ ). Cto-MET also decreased the AMPA receptor subunit GluA1 ( $P = 0.021$ ,  $n = 5$ ) and increased the NMDA receptor subunit GluN2B ( $P = 0.0088$ ,  $n = 5$ ). These detected changes exhibited greater enrichment in the PFC synaptosome fractions, which showed increased p-PAK1/2 (T423/402) ( $P = 0.0007$ ,  $n = 3$ ), increased p-Ser3 ( $P = 0.028$ ,  $n = 3$ ), and total cofilin ( $P = 0.036$ ,  $n = 3$ ) levels. There was also a marked decrease on GluA1 ( $P = 0.032$ ,  $n = 3$ ) and GluN2A ( $P = 0.016$ ,  $n = 3$ ),

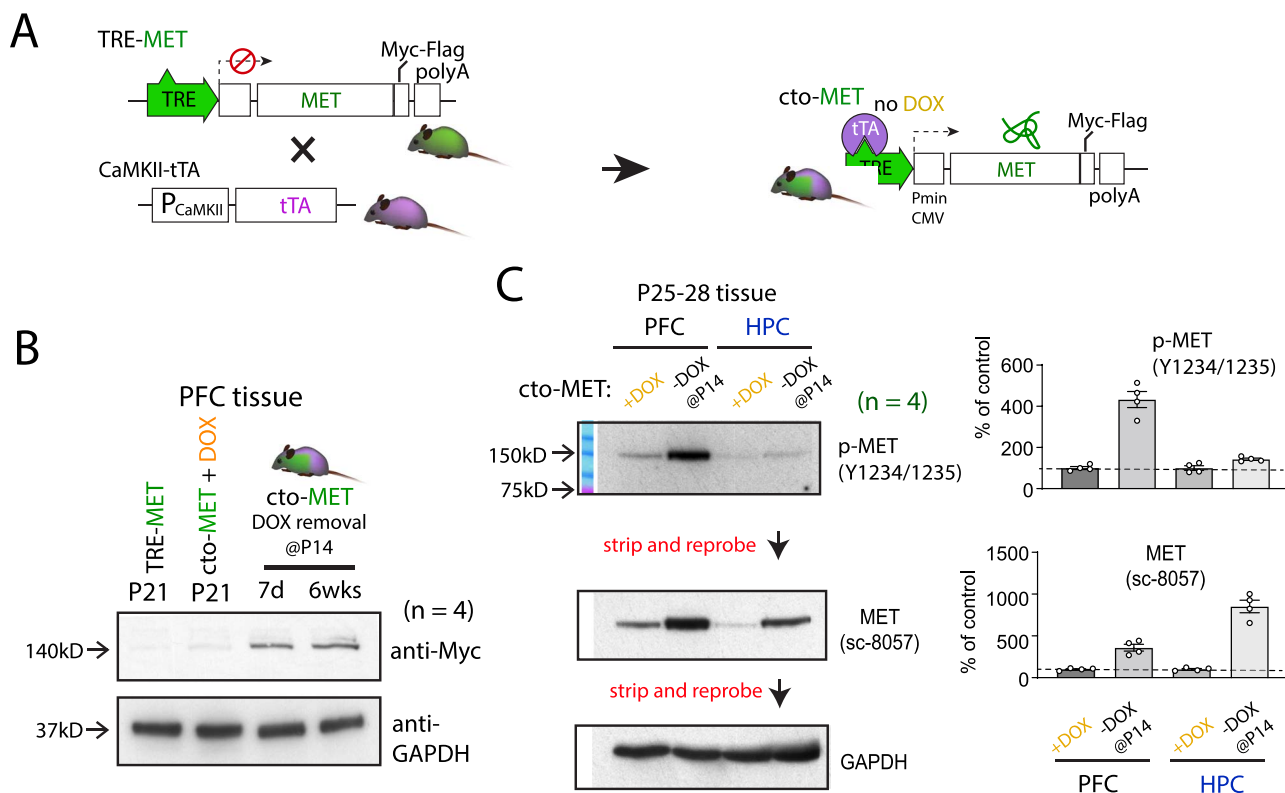


**Figure 1.** Extending MET signaling in developing cortex using a cto-MET mouse model. (A) Experimental design. TRE-MET line was crossed to the CaMKII-tTA line, which leads to transgenic MET expression in the absence of DOX. (B) No TRE-MET transgene expression was detected in the absence of tTA (top blot, lane 1). In cto-MET double transgenic mice, MET transgene expression is suppressed by DOX provided from P0 (top blot, lane 2). MET transgene is detected at 7 days and 6 weeks after DOX removal at P14 (top blot, lane 3, 4,  $n = 4$ ). (C) cto-MET leads to an increase in MET signaling, measured by pY1234/1235 in both PFC and HPC tissues. Cto-MET also exhibits elevated MET total protein ( $n = 4$ , quantification provided to the right of blot).

and increase on GluN2B ( $P = 0.018$ ,  $n = 3$ ). The observation that synaptosome preparation shows enriched levels of PSD95 and is absent in NeuN detection (Fig. 2C) indicates the validity of detected changes in above synaptic proteins. These data demonstrate that MET signaling activates the small GTPases-mediated pathway in the developing PFC that impinges on actin dynamics, through which we hypothesize that MET controls dendritic spine morphogenesis and synaptic molecular constitution (Fig. 2D).

We reasoned that if cofilin p-Ser3 phosphorylation engaged by MET signaling controls the developmental trajectory of excitatory synapse, then downregulation of MET signaling could impact the level of p-Ser3. We next investigated the temporal pattern of p-Ser3 cofilin in developing PFC in wild-type mice and found that PFC tissues exhibited a marked reduction of p-Ser3 after P21, which temporally coincides with the endogenous MET downregulation (Fig. 2E). P-Ser3 levels thereafter quickly achieved a stable, low level in P33–57 tissue. Considering MET signaling leads to increased p-Ser3, we hypothesized that downregulation of MET signaling may contribute to p-Ser3 reduction that naturally occurs as the developing cortex matures. Indeed, comparing P7 and P21 PFC tissues in *Met<sup>flx/flx::emx1<sup>cre</sup></sup>* mice (*Met<sup>ckO</sup>*) and littermate controls revealed that genetic deletion of MET signaling in the PFC led to dramatic reduction of p-Ser3 at P21, while control PFC tissues did not differ in p-Ser3 at these two ages (Fig. 2F). Taken altogether, these data show that MET signaling engages mechanisms related to spine morphogenesis and developmental maturation of synapses in PFC.

### Enhanced MET Signaling Increases Dendritic Arborization and Spine Density, but Reduces Spine Head Size in PFC Projection Neurons

Based on the molecular findings above, we asked whether timely downregulation of MET is required for normal development of neuronal morphology of prefrontal projection neurons. Deep layer cortical neurons express MET developmentally (Judson et al. 2009; Kast and Levitt 2019). To ensure meaningful comparison of the same neuronal type, we chose to study corticostriatal (CSt) L5 neurons, which form subcortical circuits, are disrupted functionally by MET (Qiu et al. 2011), and are involved in complex cognitive, social, and emotional behaviors (Peca et al. 2011; Willsey et al. 2013; Kim et al. 2016; Mei et al. 2016).

Cto-MET mice were fed with DOX-chow from P0 and switched to DOX-free chow at weaning (P21) to turn on *Met* transgene expression. We first injected retrobeads (Qiu et al. 2011) into the dorsal striatum in both cto-MET and their littermate controls at P34 and then selected the beads+ L5 CSt neurons to reveal their morphology using biocytin filling (Fig. 3A). Only CSt neurons without apparent cutoffs of apical dendrites were selected for dendritic arbor reconstruction (Fig. 3B). Sholl analysis (Sholl 1953) of dendritic length as a function of distance from soma revealed a significantly increased dendritic length distribution in cto-MET neurons (Fig. 3C,  $F_{(1,17)} = 5.35$ ;  $P = 0.034$  for genotype effect). In addition, cto-MET neurons exhibited significantly increased dendritic intersection number (Fig. 3D,  $F_{(1,17)} = 8.18$ ;  $P = 0.011$ ).

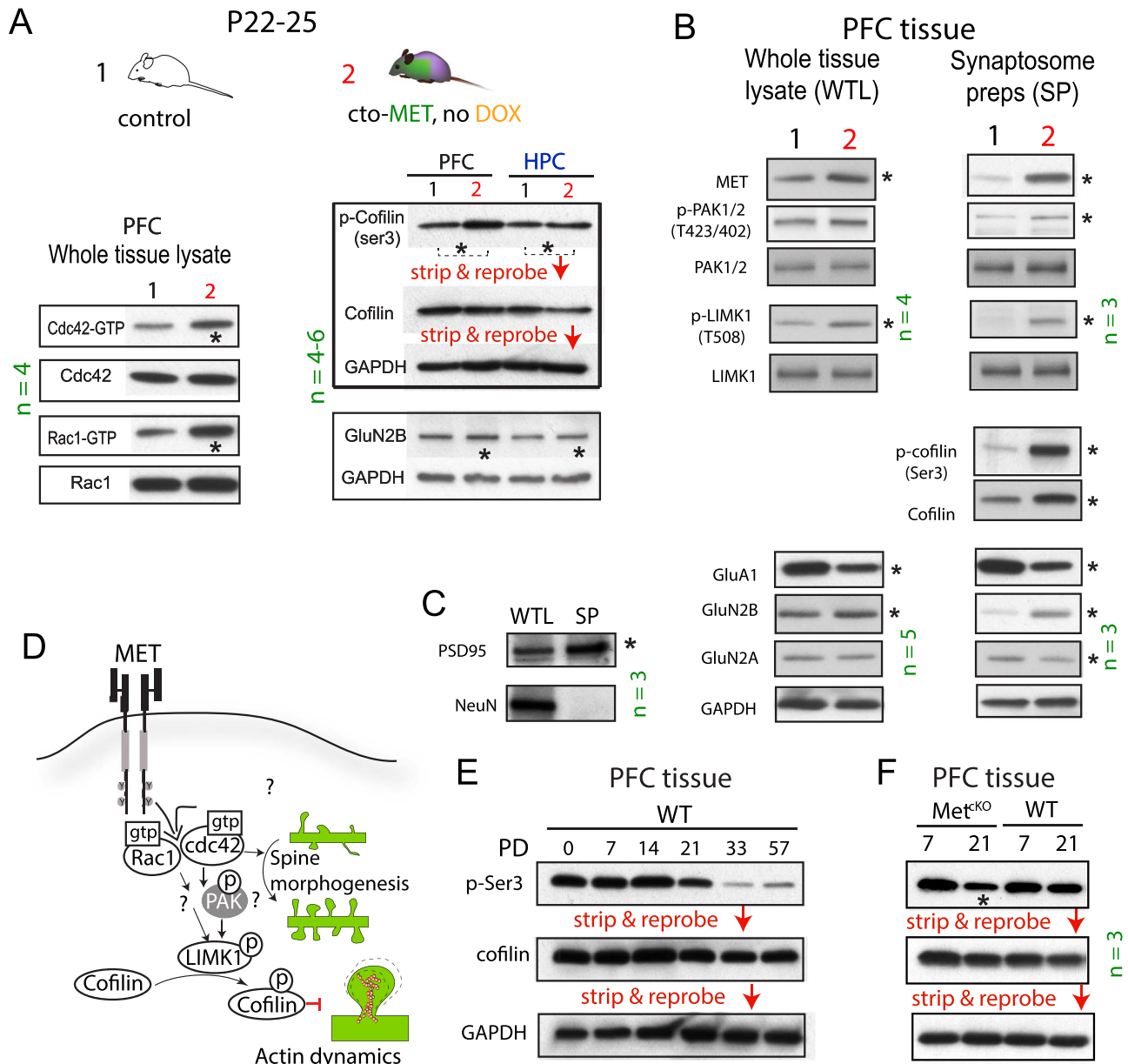


**Figure 2.** Cto-MET leads to small GTPases activation and altered profiles of synaptic proteins in the PFC. (A) cto-MET significantly increased the GTP-bound, activated forms of Cdc42 and Rac1 ( $n=4$ ) in PFC. Cto-MET also increased cofilin phosphorylation (p-Ser3), and GluN2B protein levels in PFC and HPC whole tissue lysates. Asterisks (\*) denote statistical significance ( $P < 0.05$ ). Quantification for all panels is presented in [Supplementary Figure 1](#). (B) cto-MET resulted in increased MET, p-PAK1, p-LIMK1, GluN2B, and decreased GluA1 proteins in PFC whole tissue lysates. In addition, cto-MET increased MET, p-PAK1, p-LIMK1, p-Ser3, cofilin, GluN2B, and decreased GluA1, GluN2A in the synaptosome fraction of PFC tissues. (C) A representative synaptosome prep sample shows increased PSD95 protein. In contrast, NeuN was not detected. (D) Schematic illustration connecting cto-MET signaling to actin dynamics associated with spine remodeling. (E) p-Ser3 was sharply downregulated between P21 and P33 in the PFC in WT mice ( $n=3$ ). (F) Met<sup>KO</sup> PFC tissues showed an early reduction of p-Ser3 at P21 compared with WT mice ( $n=3$ ).

We next quantified dendritic spine morphology. A representative CSt neuron dendritic segment (maximum intensity projection) and its re-reconstructed images from control and cto-MET are shown in [Fig. 3E](#). Removing DOX at P21 to allow cto-MET signaling for two weeks resulted in a significant increase in spine density ([Fig. 3F](#); number per 10  $\mu\text{m}$ : control,  $10.35 \pm 0.47$ ; cto-MET,  $13.89 \pm 0.45$ ;  $t_{(33)} = 5.3$ ,  $P < 0.0001$ ). In addition, there was a significantly increased spine length distribution for cto-MET neurons ([Fig. 3G](#),  $D = 0.277$ ,  $P < 0.0001$ ; control,  $n = 268$  spines from 8 neurons/5 mice; cto-MET,  $n = 278$  spines from 7 neurons/5

mice). Based on classic morphometric parameters, we further classified spines into four categories: “filopodia,” “stubby,” “mushroom,” and “long thin” ([Peng et al. 2016](#)). We found that cto-MET had a significant effect on spine classification ([Fig. 3H](#),  $F_{(1,100)} = 45.4$ ,  $P < 0.0001$ . Two-way ANOVA); whereas cto-MET increased the number of “filopodia,” “stubby,” and “long thin” immature type of spines, the number of “mushroom” type of mature spines was significantly reduced ([Fig. 3H](#),  $P < 0.0001$  for genotype comparison within each category, Sidak’s MCT). The data indicate that cto-MET accumulation well beyond

the normal period of endogenous receptor expression has a dramatic effect on L5 PFC dendritic arborization and spine maturation.

### Extended Signaling of MET in Prefrontal Projection Neurons Alters Synaptic Activity

The increased spine density, length, and decreased mushroom type of spines collectively indicate that L5 CSt neurons maintain an immature phenotype as a result of extending MET expression. We next asked whether timely downregulation of MET is required for normal development of synaptic activity and functional maturation in PFC CSt neurons. Cto-MET and control mice were fed with DOX chow from P0, switched to DOX-free chow at P21, and sacrificed for recording at P35–40. This results in transgenic MET signaling for approximately two additional weeks. Bead+ CSt L5 neurons in PFC slices were voltage-clamped to record the spontaneous mEPSC activities (Fig. 4A). cto-MET neurons exhibited overall smaller mEPSC amplitude (Fig. 4B. Test on cumulative distribution,  $P < 0.001$ , K-S test. Control,  $n = 1135$  events/11 cells/5 mice; cto-MET,  $n = 1293$  events/12 cells/6 mice). In contrast, cto-MET neurons showed a significant increase in mEPSC frequency (Fig. 4C. Control,  $2.66 \pm 0.25$  events/s; cto-MET,  $3.94 \pm 0.31$  events/s,  $t_{(27)} = 3.29$ ,  $P = 0.0028$ ), potentially reflecting weaker yet more numerous inputs. We next recorded mIPSC activity in these neurons (Fig. 4D) and found that cto-MET did not alter either mIPSC amplitude (Fig. 4E,  $P = 0.68$ , K-S test. Control,  $n = 887$  events/10 cells/5 mice; cto-MET,  $n = 1130$  events/11 cells/6 mice) or mIPSC frequency (Fig. 4F; control,  $3.86 \pm 0.40$  events/s; cto-MET,  $4.24 \pm 0.43$  events/s,  $t_{(27)} = 0.63$ ,  $P = 0.53$ ). These results are consistent with the cto-MET-induced immature spine morphology of CSt L5 neurons and suggest that extending MET expression leads to a combined decrease in spine maturation and altered synaptic inputs.

Excitatory synapse maturation is also reflected by a temporal increase in AMPA receptor content, rendering the immature “silent synapse” functional (Liao et al. 1995; Harlow et al. 2010; Huang et al. 2015). To investigate whether extending MET expression disrupts this process, we next measured AMPA/NMDA receptor current ratio (A:N) by stimulating the L2/3 inputs (Fig. 4G) and recording whole-cell synaptic currents in L5 CSt neurons. Consistent with an immature phenotype, cto-MET neurons exhibited a significantly reduced A:N ratio (Fig. 4H; control,  $1.45 \pm 0.08$ ,  $n = 13$ ; cto-MET,  $1.14 \pm 0.08$ ,  $n = 13$ ,  $t_{(24)} = 2.79$ ,  $P = 0.010$ ). These data indicate that cto-MET leads to both structural and functional cellular phenotypes that are consistent with disrupted developmental maturation of L5 CSt PFC neurons.

### Sustained MET Expression Alters Prefrontal Cortical Circuit Connectivity

We next asked whether cto-MET changes the interlaminar, local synaptic connectivity of L5 CS neuron. PFC L5 projection neurons receive major synaptic inputs from L2/3, in addition to weaker inputs from other layers and neuronal types (Dembrow and Johnston 2014; Dembrow et al. 2015; Markram et al. 2015). We used LSPS mapping (Shepherd and Svoboda 2005; Suter et al. 2010; Qiu et al. 2011) to quantify synaptic inputs made onto PFC L5 CSt neurons (Fig. 5A,B). Control and cto-MET mice were sacrificed at P35–40 and sagittal PFC slices were made. Bead+ L5 CSt neurons were first voltage-clamped at  $-70$  mV to obtain excitatory synaptic currents in responses to glutamate uncaging

at  $16 \times 16$  locations (Fig. 5C) and then at 0 mV to obtain inhibitory responses (Fig. 5D).

After collecting multiple LSPS maps in each group, averaged excitatory maps revealed that control L5 CSt neurons receive strong inputs from L2/3 location (Fig. 5E). Compared with control CSt neurons, L2/3 inputs to cto-MET CSt neurons were markedly altered. Although quantification of inputs did not exhibit altered overall laminar excitatory synaptic connectivity (Fig. 5F, main effects on genotype,  $F_{(1,416)} = 1.10$ ,  $P = 0.29$ ), the averaged inputs from combined L2/3 locations showed a significant reduction (Fig. 5G; control,  $29.1 \pm 3.38$  pA; cto-MET,  $20.0 \pm 1.69$  pA,  $t_{(28)} = 2.58$ ,  $P = 0.015$ ). Surprisingly, cto-MET L5 CSt neurons received significantly stronger inputs from L5 locations (Fig. 5H; control,  $4.92 \pm 1.34$  pA; cto-MET,  $11.45 \pm 2.32$  pA,  $t_{(28)} = 2.34$ ,  $P = 0.033$ ). These altered laminar inputs suggest that connectivity onto L5 neurons is changed with sustained MET signaling. We next quantified the inhibitory connectivity. L5 CSt neurons receive major inhibitory inputs from both L5 and L2/3 locations (Fig. 5I). No effect on genotype was found for the overall laminar inhibitory connectivity (Fig. 5J. Main effects on genotype,  $F_{(1,496)} = 1.64$ ,  $P = 0.20$ ). In addition, comparison of combined averaged inhibitory inputs from L2/3 and L5 also revealed no statistical significance (Fig. 5K; control,  $69.01 \pm 4.94$  pA; cto-MET,  $66.86 \pm 5.52$  pA,  $t_{(31)} = 0.28$ ,  $P = 0.77$ ). Therefore, sustained MET signaling in PFC L5 neurons results in altered synaptic connectivity, which likely disrupts the integration of different input sources and outputs of these projection neurons.

### Decreased Spine Pruning Contributes to Increased Spine Density in Visual Cortex Projection Neurons

The cto-MET-induced increase in spine density and inhibitory phosphorylation of the actin-binding protein cofilin suggest that extending MET signaling may result in disrupted spine dynamics and pruning. Therefore, we performed *in vivo* spine imaging to determine whether the increased spine density may be a result of increased spine production or decreased spine pruning. We crossed the cto-MET mice with the Thy1-GFP line (Feng et al. 2000) and conducted repeated two photon imaging on dendritic spines in the primary visual cortex (V1) of cto-MET::Thy1 mice and their littermate control mice that do not express the TRE-MET transgene (Fig. 6A). Because mPFC is not readily accessible for repeated *in vivo* imaging, we turned to a more technically tractable cortical area, V1, which has similar temporally controlled MET expression patterns to mPFC (Judson et al. 2009; Judson et al. 2011; Kast and Levitt 2019), and exhibits altered critical period maturation due to extended MET signaling (Chen et al. 2020). Considering MET signaling engages conserved molecular mechanisms impinge on the spine dynamics, we reason that the effects of cto-MET on spines in V1 may be conserved and applicable to mPFC circuits. We adopted a thinned skull preparation (Fig. 6B) (Yang et al. 2010; Yu and Zuo 2014) to minimize the potential activation of microglia, which can affect synapse development (Parkhurst et al. 2013; Schafer and Stevens 2013; Zhan et al. 2014). Two imaging sessions were carried out (Fig. 6C), one each at P25 and P32. Dendritic spine formation and elimination during the one-week period was measured.

We designed two experimental groups using cto-MET::Thy1-GFP mice (Fig. 6C); the first group received DOX chow from P0 but switched to DOX-free chow at P14 to turn on cto-MET. The second experimental group (cto-MET<sup>ON/OFF</sup>) was designed to examine the effect of turning off MET signaling on spine dynamics, in which cto-MET mice were fed regular



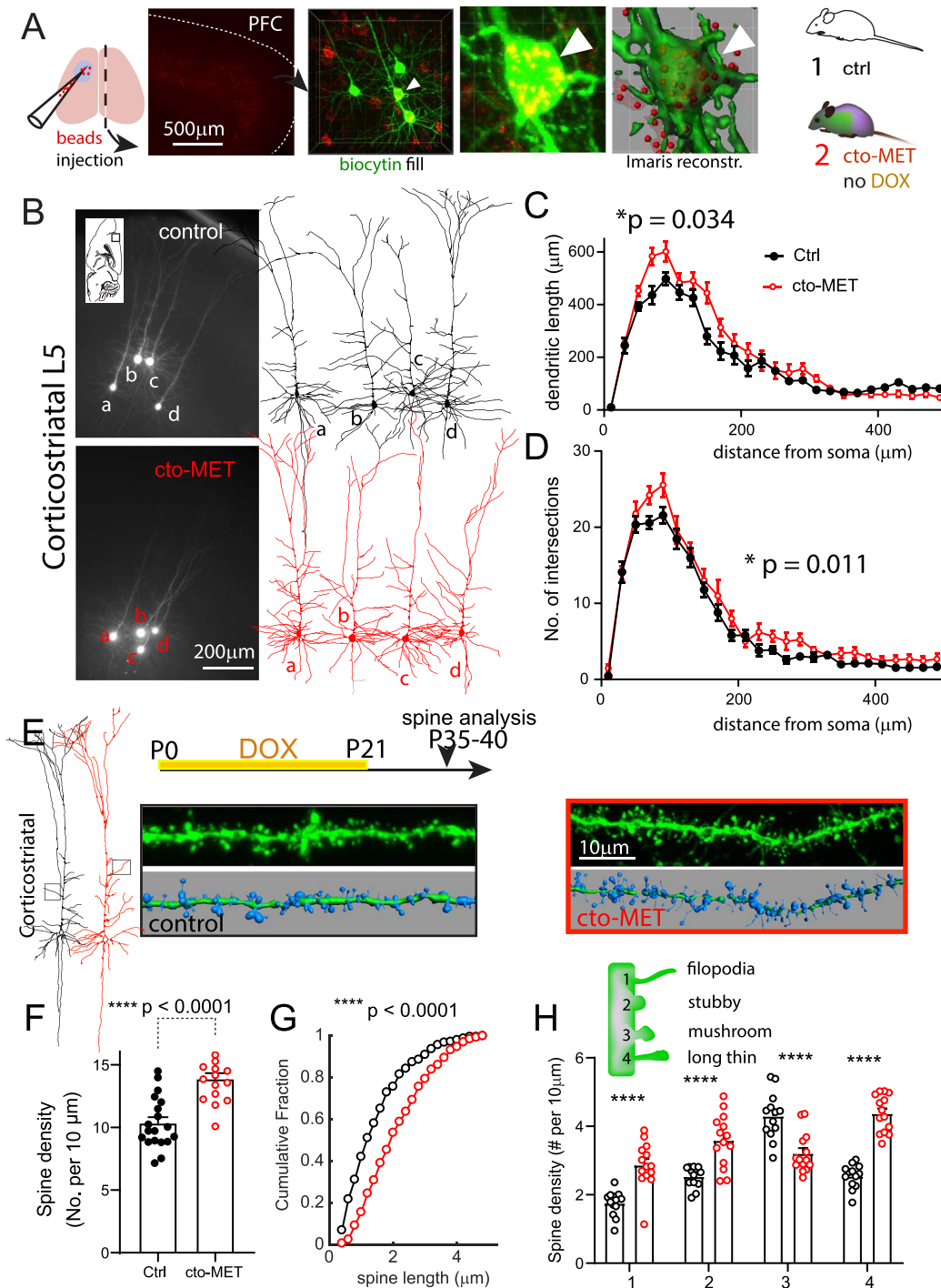


**Figure 3.** Sustained MET signaling increases dendritic branching and spine density in PFC Cst neurons. (A) Selective labeling of Cst neurons by retrobeads. (B) Biocytin filling and representative dendritic arbor reconstruction in cto-MET and control PFC L5 Cst neurons. (C) Sholl analysis on dendritic length as a function of distance from soma. Main effect on group,  $F_{(1,17)} = 5.35$ ;  $*P = 0.034$ . (D) Sholl analysis on number of dendritic intersections. Main effect on group,  $F_{(1,17)} = 8.18$ ;  $*P = 0.011$ . (E) Representative MIP images of dendritic spines and 3D reconstructions from control and cto-MET Cst neurons. (F) cto-MET significantly increased spine density.  $t_{(33)} = 5.3$ ,  $****P < 0.0001$ . (G) cto-MET significantly increased spine length.  $****P < 0.0001$ . (H) cto-MET significantly changed spine categorical distribution in Cst PFC neurons.  $F_{(1,100)} = 45.4$ ,  $****P < 0.0001$ .

chow from P0 but were switched to DOX-chow at P21 to suppress MET signaling. Control mice (tTA:Thy1-GFP) were fed with DOX chow from birth and throughout the experiment. Overall, disrupting MET signaling during the normal period of pruning significantly altered spine dynamics (Fig. 6D). Main

effect on group:  $F_{(2,33)} = 13.99$ ;  $P < 0.0001$ ). Compared with the spine formation rate in control mice ( $10.69 \pm 1.52\%$ ,  $n = 11$  mice), cto-MET exhibited a significant increase in the rate of spine formation ( $15.00 \pm 1.28\%$ ,  $P = 0.031$ ; Dunnett's multiple comparison test,  $n = 12$  mice), whereas cto-MET<sup>ON/OFF</sup> led to a

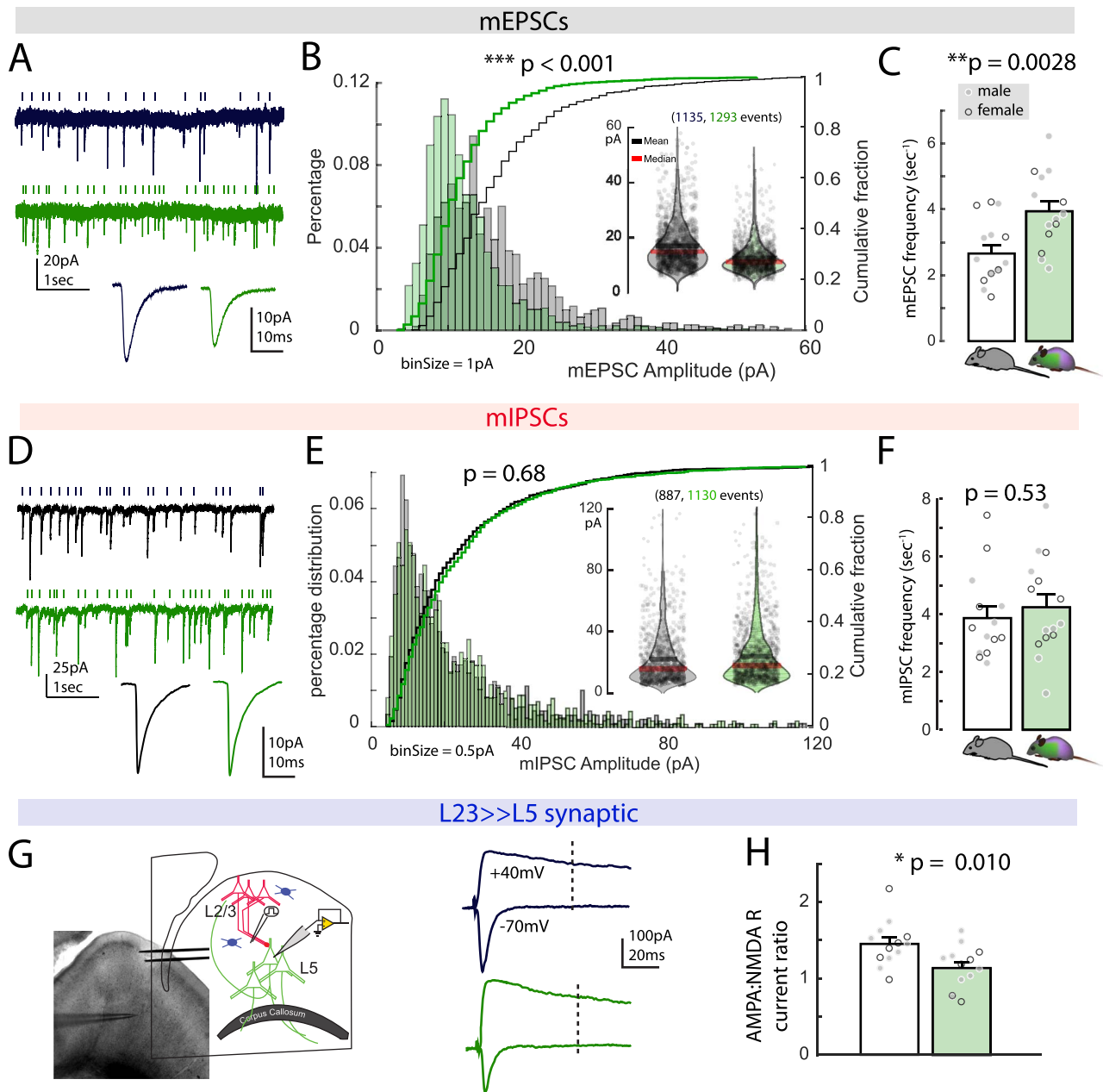


**Figure 4.** cto-MET leads to altered synaptic activity and maturation of L5 CST neurons in the PFC. (A) Sample mEPSC recordings from control and cto-MET L5 CST neurons. Vertical ticks indicate timestamps of detected mEPSCs. (B) Histogram and cumulative distribution of mEPSC amplitudes from control and cto-MET L5 CST neurons. \*\*\* $p < 0.001$ , K-S test. **Inset**, scatter plot of analyzed mEPSC amplitudes. (C) cto-MET increased mEPSC frequency.  $t_{(27)} = 3.29$ , \*\* $p = 0.0028$ . (D) Sample mIPSC responses from control and cto-MET L5 CST neurons. (E) Histogram and cumulative distribution of mIPSC amplitudes. Cto-MET did not change cumulative mIPSC amplitude distribution.  $P = 0.68$ , K-S test. (F) cto-MET had no effect on mIPSC frequency.  $t_{(27)} = 0.63$ ,  $P = 0.53$ . (G) Illustration of measurement of AMPA/NMDA receptor current ratio at the L2/3 > L5 synapse. (H) cto-MET significantly reduced AMPA/NMDA receptor current ratio.  $t_{(24)} = 2.79$ , \* $P = 0.010$ .

significant decrease in the rate of spine formation ( $6.33 \pm 0.73\%$ ,  $P = 0.026$ ;  $n = 13$  mice). Altered cto-MET signaling also disrupted normal spine elimination dynamics ( $F_{(2,33)} = 19.42$ ;  $P < 0.0001$ ). Compared with the spine elimination rate in control mice ( $10.19 \pm 1.03\%$ ), cto-MET exhibited a significant decrease in the rate of spine elimination ( $6.56 \pm 0.78\%$ ,  $P = 0.014$ ). In contrast, cto-MET<sup>ON/OFF</sup> exhibited a significant increase in the rate of spine elimination ( $14.13 \pm 0.79\%$ ,  $P = 0.006$ ). Together, these in vivo longitudinal imaging data strongly suggest that temporally controlled MET signaling regulates spine dynamics and pruning.

### Briefly Extending MET Signaling for 2 Weeks in Juvenile Cortex Leads to Select Behavioral Disruption in Adult Mice

The data thus far demonstrate that sustaining MET expression for two weeks after downregulation of the endogenous signaling leads to altered biochemical, morphological, and electrophysiological maturation of L5 Cst neurons. These changes may account for altered synaptic activity and circuit connectivity (Geschwind and Levitt 2007; Rudie et al. 2012; Hong et al. 2019; Maximo and Kana 2019). The influence of the highly controlled

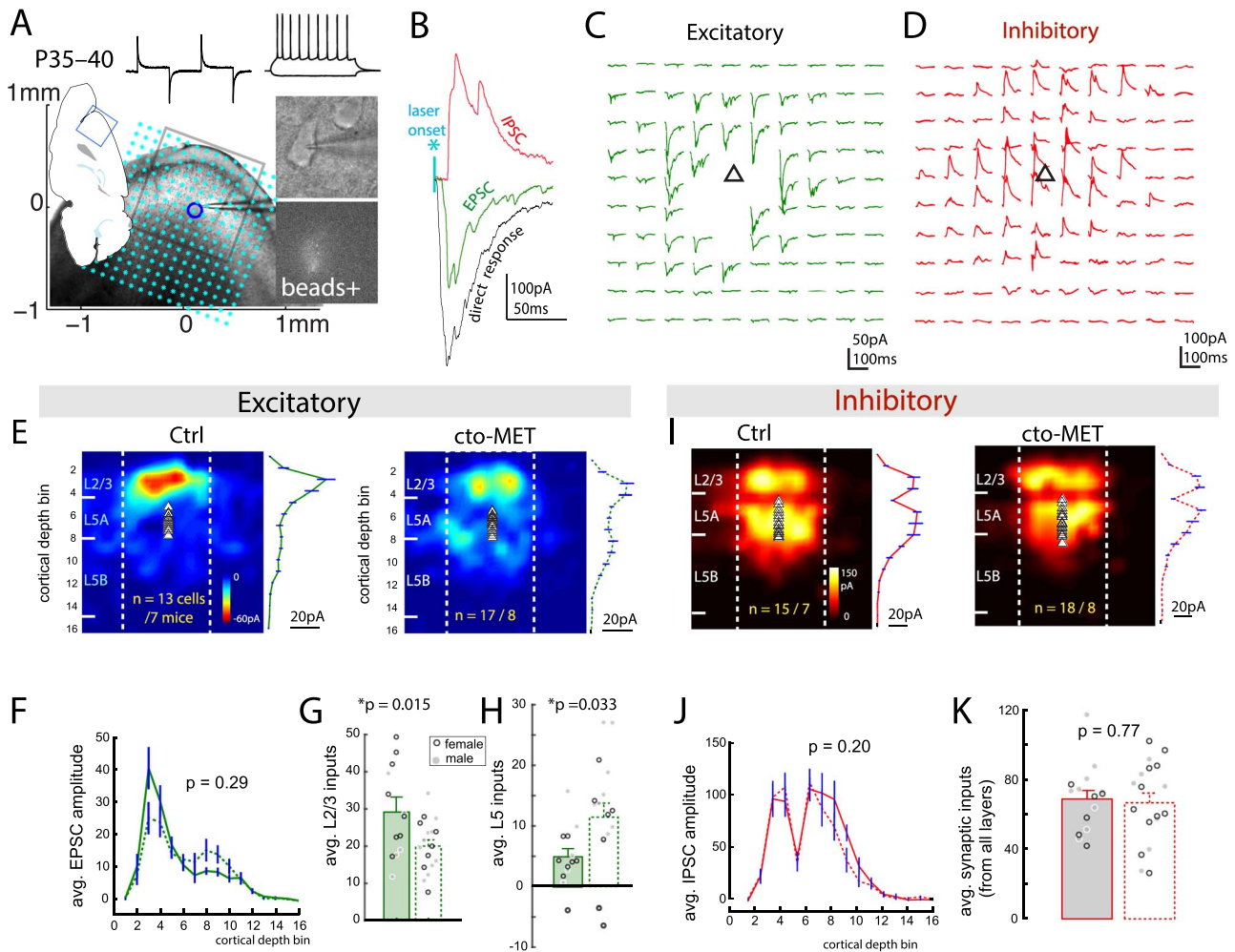


**Figure 5.** cto-MET leads to altered intracortical circuit connectivity. (A) Schematic illustration of a parasagittal PFC slice and whole-cell recordings on beads+ L5 CSt. Inset indicates test pulses to obtain neuronal membrane properties. Cyan asterisks indicate glutamate uncaging locations. (B) Laser uncaging at different locations induces direct soma responses and synaptic EPSCs/IPSCs. (C) Representative excitatory synaptic responses at the central  $10 \times 10$  locations (gray box in A) from a L5 CSt neuron. (D) Representative inhibitory synaptic responses at the same location from the same CSt neuron. (E) Averaged excitatory synaptic input maps to L5 CSt neurons from control ( $n = 13$  cells/7 mice) and cto-MET ( $n = 17$  cells/8 mice) groups. (F) Quantification of averaged synaptic input strength (quantified using the middle eight columns) as a function of laminar location did not reveal an overall effect of groups.  $F_{(1,416)} = 1.10$ ,  $P = 0.29$ . (G) Comparison of average combined excitatory inputs from L2/3 location.  $t_{(28)} = 2.58$ ,  $*P = 0.015$ . (H) Comparison of averaged excitatory synaptic inputs from L5 location.  $t_{(28)} = 2.34$ ,  $*P = 0.033$ . (I) Averaged inhibitory synaptic input maps to L5 CSt neuron from control ( $n = 15$  cells/7 mice) and cto-MET ( $n = 18$  cells/8 mice) groups. (J) Quantification of averaged inhibitory synaptic input strength as a function of laminar location.  $F_{(1,496)} = 1.64$ ,  $P = 0.20$ . (K) Quantification of averaged inhibitory synaptic inputs from combined L2/3 and L5 locations.  $t_{(31)} = 0.28$ ,  $P = 0.77$ .

timing of MET signaling in subsets of cortical neurons ultimately may modulate the plasticity and function of circuits that express the receptor developmentally and impinges on behavior. To address this, cto-MET mice were fed DOX chow until P21 and then switched to DOX-free chow for two weeks, through puberty before switching back to DOX chow to turn off cto-MET. Littermate mice with no TRE-MET transgene but with the same DOX chow regimen served as the control group (Fig. 7A). We then conducted a battery of behavior tasks at 16–20 weeks, corresponding to young adults.

Mice were first scored for exhibiting repetitive behaviors in their home cage. Compared with controls, cto-MET mice showed significantly altered repetitive behavior profiles (Fig. 7B; main group effect:  $F_{(1,81)} = 27.7$ ,  $P < 0.0001$ ; interaction,  $F_{(2,81)} = 9.98$ ,  $P = 0.0001$ ). Specifically, cto-MET mice spent increased time digging (control,  $18.5 \pm 3.4$  s,  $n = 14$  mice; cto-MET,  $58.8 \pm 10.1$  s,

$n = 15$  mice,  $P = 0.038$ ) and jumping (control,  $8.6 \pm 2.0$  s; cto-MET,  $110.1 \pm 23.5$  s,  $P < 0.0001$ ). In addition, cto-MET mice exhibited increased marble burying (Fig. 7C; number of marbles buried: control,  $3.57 \pm 0.56$ ; cto-MET,  $6.20 \pm 0.72$ ,  $P = 0.009$ , Mann-Whitney U test). cto-MET mice showed no difference in repetitive grooming (Fig. 7B; total time spent in grooming during a 30-min session: control,  $35.4 \pm 4.35$  s; cto-MET,  $37.8 \pm 4.0$  s; two-way ANOVA with Sidak's MCT,  $P = 0.99$ ). The increase in the subset of repetitive behaviors is not due to an increase in basal locomotor activity, as cto-MET mice perform similarly in the OF test (Fig. 7D) in terms of total distance traveled (Fig. 7E; control,  $49.2 \pm 3.58$  m; cto-MET,  $46.3 \pm 2.94$  m,  $t_{(27)} = 0.64$ ,  $P = 0.53$ ).

We next asked whether cto-MET alters anxiety levels. One measure is the amount of time in the center compared with walls of the OF. There were no differences between control and cto-MET mice (Fig. 7F; control,  $49.5 \pm 5.8$  s; cto-MET,  $50.2 \pm 7.9$  s,

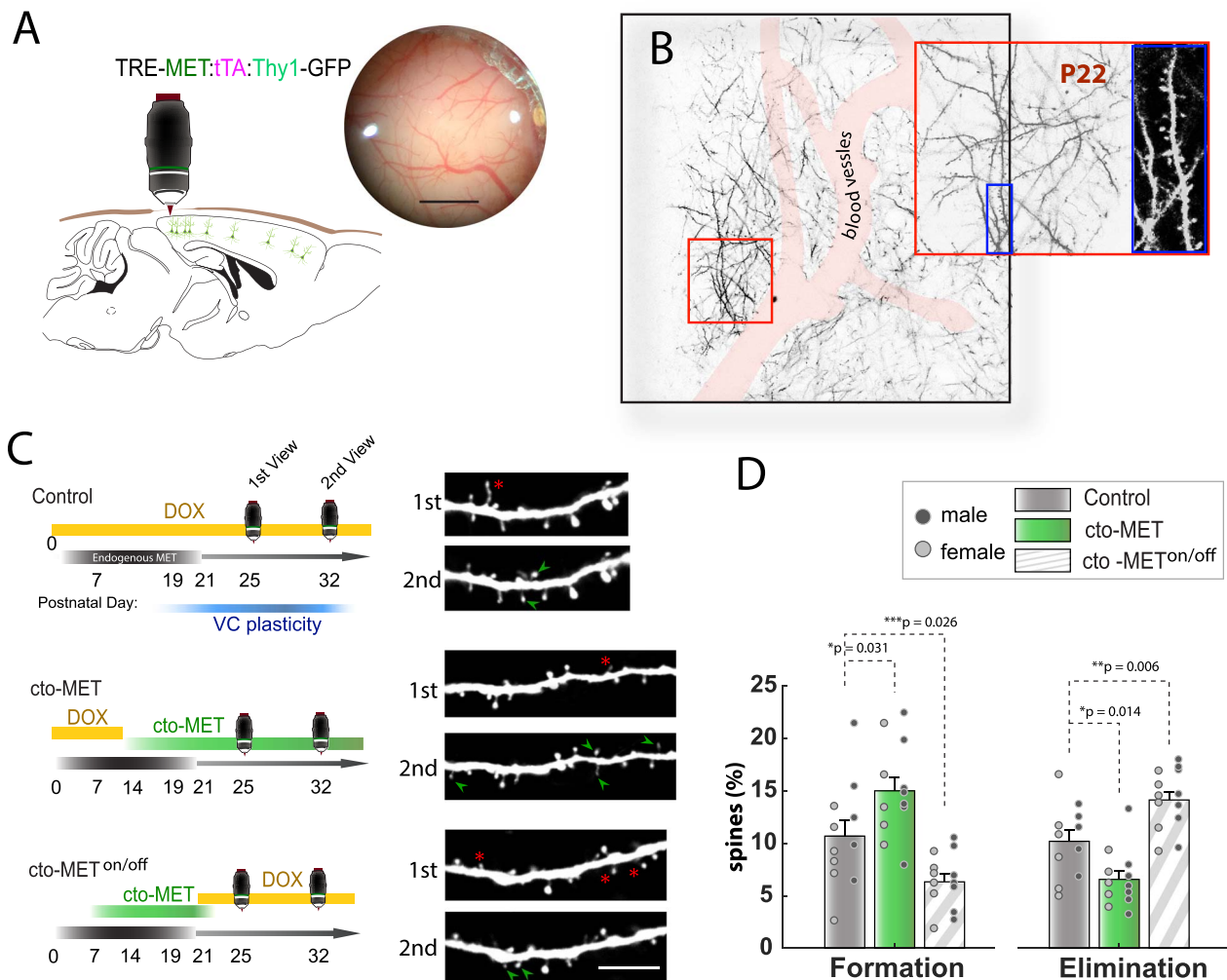


**Figure 6.** cto-MET leads to impaired dendritic spine developmental pruning. (A) Illustration of chronic two-photon dendritic spine imaging using a thinned skull preparation. (B) A representative FOV of spine imaging in V1, which allows identification of the same dendritic segment based on vasculature landmarks. (C) Experimental design of three groups, and their representative spine images at P25 and P32. Green arrow, spine formation; red cross, spine elimination. (D) Quantification of spine formation and spine elimination during the 1-week period. cto-MET significantly increased spine formation (\* $P = 0.031$ ), whereas cto-MET<sup>ON/OFF</sup> led to reduced formation (\* $P = 0.026$ ). In contrast, cto-MET significantly decreased (\* $P = 0.014$ ), while cto-MET<sup>ON/OFF</sup> significantly increased (\*\* $P = 0.006$ ) spine elimination.

$t_{(27)} = 0.07$ ,  $P = 0.94$ ) during the 10-min test. Mice were next assessed on the EPM (Fig. 7G). Cto-MET mice exhibited similar open arm entries (Fig. 7H; control,  $5.71 \pm 0.9$ ; cto-MET,  $6.20 \pm 0.63$ ,  $P = 0.48$ , Mann-Whitney test) and the amount of time spent in the open arm (Fig. 7I; control,  $38.5 \pm 3.8$  s; cto-MET,  $34.4 \pm 4.8$  s,  $t_{(27)} = 0.69$ ,  $P = 0.49$ ).

To examine sociability and social novelty, the mice were run in a three-chamber social interaction test (Fig. 7J), which was conducted in three phases (Silverman et al. 2010; Rein et al. 2020). cto-MET mice differed significantly in their overall social preference index (SPI) score across the three phases (Fig. 7K; main effect of group,  $F_{(1,81)} = 30.5$ ,  $P < 0.0001$ , Two-way ANOVA). While cto-MET mice did not show preference over two different nonsocial objects (phase 1, SPI: control,  $0.031 \pm 0.035$ ; cto-MET,  $0.091 \pm 0.027$ ,  $P = 0.28$ , Sidak's MCT), they exhibited a significantly lower SPI in the phase 2 test (Fig. 7K; control,  $0.50 \pm 0.022$ ; cto-MET,  $0.15 \pm 0.021$ ,  $P < 0.0001$ , Sidak's MCT), during which an unfamiliar mouse and inanimate object were presented. In addition, cto-MET showed a decreased SPI toward a stranger mouse

(Soc2) over a familiar mouse (Soc1) in phase 3 test, indicative of impaired social novelty (Fig. 7K; Control,  $0.241 \pm 0.019$ ; cto-MET,  $0.127 \pm 0.036$ , Two-way ANOVA with Sidak's MCT,  $P = 0.021$ ). We also quantified total time spent in interaction with the social and nonsocial object during phase 2 (Fig. 7L). Cto-MET mice significantly differ in their overall time spent investigating Soc1 and NS object ( $F_{(1,54)} = 14.85$ ,  $P = 0.0003$ ); whereas control mice clearly demonstrated an increased time in interacting with social subject (Soc1,  $143.6 \pm 8.4$  s; NS,  $55.4 \pm 4.4$  s,  $P < 0.0001$ , Two-way ANOVA with Sidak's MCT), cto-MET mice exhibited no preference for the Soc1 social subject (Soc1,  $73.8 \pm 19.1$  s; NS,  $82.5 \pm 21.3$  s,  $P = 0.45$ ). These data indicate that extending MET signaling during the adolescent period results in long-lasting changes of a subset of adult behaviors, including social behavior.

## Discussion

The current study uses a novel transgenic mouse with regulatory capabilities, combined with an interdisciplinary approach, to



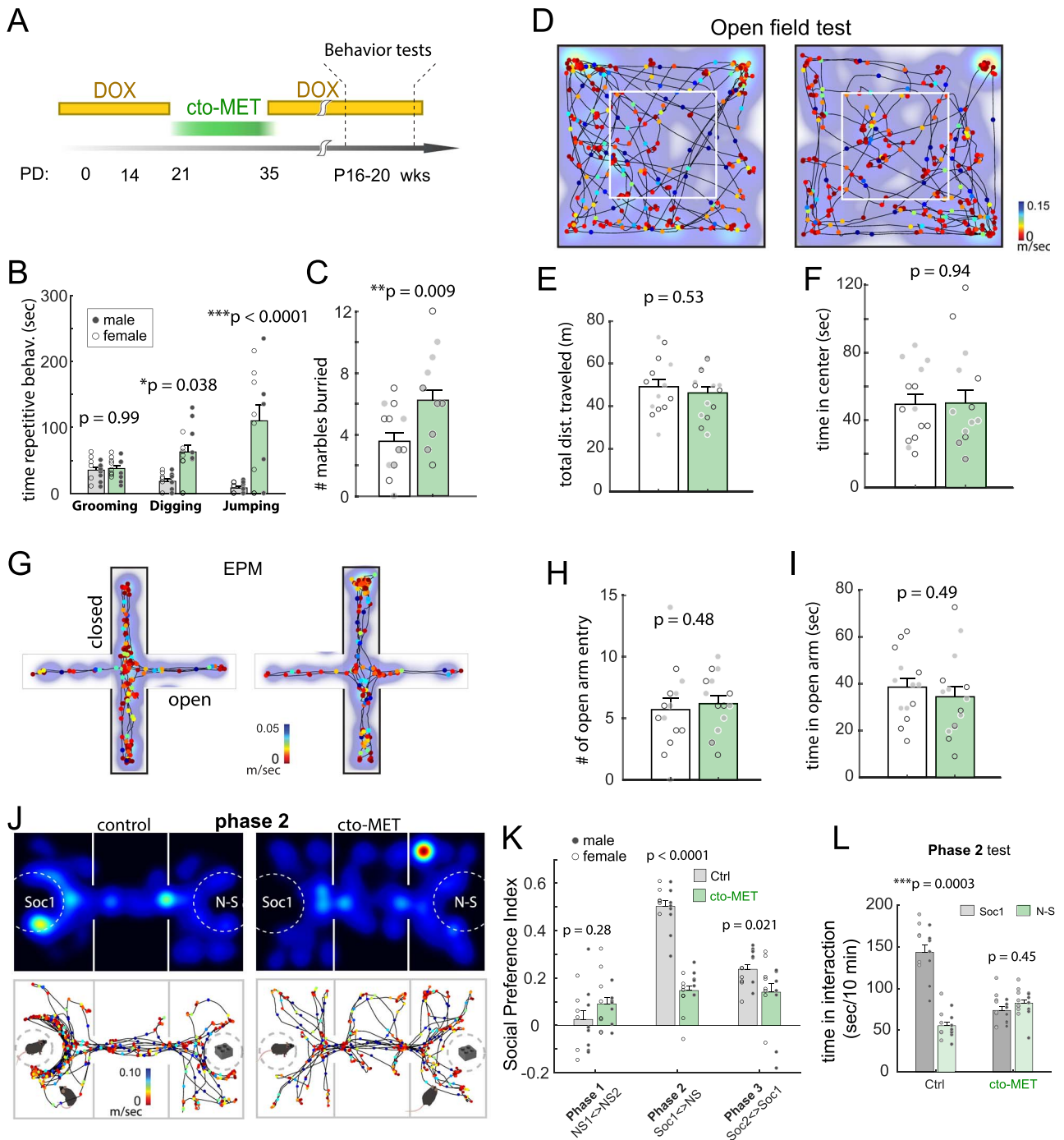


**Figure 7.** Cto-MET in developing cortex leads to select behavioral changes in adults. (A) Experimental paradigm for cto-MET. cto-MET was turned on briefly to extend/enhance MET signaling for two weeks (P21–35). (B) cto-MET increased digging ( $*P = 0.038$ ) and jumping ( $***P < 0.0001$ ) behaviors in young adult mice. (C) cto-MET increased repetitive marble-burying behaviors in young adult mice ( $**P = 0.009$ ). (D) Representative heatmaps and moving tracks/speed in an OF test of control and cto-MET mice. (E) cto-MET did not alter the distance traveled during the 10-min OF test.  $t_{(27)} = 0.64$ ,  $P = 0.53$ . (F) cto-MET did not alter the time spent in center of the open field.  $t_{(27)} = 0.07$ ,  $P = 0.94$ . (G) Representative heatmaps and moving track/speed in an EPM test. (H) cto-MET did not alter the number of open arm entries ( $P = 0.48$ ). (I) cto-MET did not alter the time spent in the open arm ( $t_{(27)} = 0.69$ ,  $P = 0.49$ ). (J) Representative heatmaps and moving track/speed in the phase 2 of the three-chamber social interaction test. (K) cto-MET did not affect SPI in phase 1 ( $P = 0.28$ ), but reduced SPI significantly during phase 2 ( $P < 0.0001$ ) and phase 3 ( $P = 0.021$ ) tests. (L) Control mice spent significantly more time interacting with Soc1 over the N-S object ( $***P = 0.0003$ ). In contrast, cto-MET did not exhibit such a preference ( $P = 0.45$ ).

identify a signaling mechanism through which maturation of excitatory synaptic connectivity and function occur in the cerebral cortex. Here, experiments reveal that normal timing of MET signaling is a critical molecular determinant of circuit

maturation in the postnatal PFC. A convergence of data shows that sustained MET signaling past the time of its normal decline is sufficient to alter neuronal dendritic structure, spines morphology, biochemical maturation of synapses, physiological

maturation of intracortical circuits, and the emergence of repetitive motor and social behaviors that involve PFC-related circuitry.

Receptor tyrosine kinases play key roles in mediating histogenic events in the developing brain (Hausott et al. 2009; Park and Poo 2013; Wittkowski et al. 2014). Unlike many other RTKs, one key feature of MET signaling in cortical circuits, which is conserved in all species examined thus far (Judson et al. 2009; Judson et al. 2011; Mukamel et al. 2011), is that receptor activity is largely restricted to late prenatal and early postnatal periods. In rodents, this occurs in the first 2–3 weeks after birth, during which MET has been shown to promote neuronal dendritic morphology and synaptogenesis (Gutierrez et al. 2004; Qiu et al. 2014; Eagleson et al. 2016; Peng et al. 2016; Xie et al. 2016). In the adult mouse brain, a much lower level of MET is located at both presynaptic and postsynaptic compartments (Eagleson et al. 2013) but is capable of modulating mature synapse function and plasticity (Akimoto et al. 2004). The effect of MET signaling on neuronal morphology is observed in cultured cortical and hippocampus neurons (Qiu et al. 2014; Eagleson et al. 2016; Xie et al. 2016), suggesting that cell-autonomous mechanisms in dorsal pallial neurons are involved in modulating morphological development. Intriguingly, abrupt downregulation of MET signaling precedes the peak of synapse pruning, functional maturation, and refinement of connectivity (Eagleson et al. 2016). Disruption of this pattern of signaling, such as that occurs in mice with conditional knockout of *Met* gene, leads to altered maturation and a major disruption of the timing of critical period plasticity in the visual cortex induced by monocular deprivation (Chen et al. 2020). Utilizing the unique cto-MET model, we now report that extending MET signaling for a brief period in developing cortical circuits leads to disrupted molecular signaling networks, leading to activation of the small GTPases Rac1, Cdc42, and persistent inhibition of the actin depolymerizing factor cofilin. These molecular adaptations are consistent with the observed disruption of mature spine formation and the elimination during a specific time window of cortical circuit development.

Normal MET expression in developing PFC is temporally regulated in subsets of superficial and deep layer excitatory neurons (Judson et al. 2009). Here we used a tTA mouse line to drive cto-MET broadly in excitatory neurons, which may result in MET<sup>+</sup> neurons that normally don't express the receptor. Nevertheless, the temporally regulated cto-MET expression approach adopted here, although artificial, reveals that dysregulation of the receptor temporally during development is sufficient to impact neuronal maturation at multiple levels. While studies of postmortem human brain of individuals with neurodevelopmental disorders do not provide direct information on key dysregulated molecular pathways during late prenatal and early postnatal periods of extensive neuronal and synapse growth, many of the causal genes are powerful regulators of pathways involved in neurogenesis and neuronal and synaptic maturation (Harlow et al. 2010; Gandal et al. 2018; Li et al. 2018; Ramaswami et al. 2020; Searles Quick et al. 2021). MET signaling is pleiotropic, capable of engaging multiple pathways that cross talk with many key developmental hub genes implicated in neurodevelopmental disorders. For example, MET signaling intersects FOXP2 and MeCP2 (Mukamel et al. 2011; Plummer et al. 2013), which likely modifies broad developmental milestones of forebrain circuits. MET is well-known to be pleiotropic (Peng et al. 2016), interacting with molecular regulators of neuronal survival in motor neurons (Novak et al. 2000; Genestine et al. 2011; Lamballe et al. 2011), as well as synapse formation and

neuronal maturation, such as shown here with small GTPases, as well as ERK and PI3 kinase intracellular signaling pathways (Eagleson et al. 2016).

Importantly, we found dramatic effects imparted by mistimed MET signaling on cortical circuit development, revealed by a number of measures that use different methods that consistently demonstrated an altered maturational trajectory. Sustained MET signaling for two weeks following in vivo downregulation of MET leads to elevated spine density, reduced spine size, increased spontaneous synaptic inputs of weaker amplitudes, and disrupted topology of intracortical connectivity. Specifically, L5 CSt neurons show smaller yet more numerous number of spines, which is consistent with the measures of more frequent mEPSCs of smaller amplitudes. These excitatory synapses in cto-MET mice may be bridled in an immature state, consistent with the decreased A:N ratio, increased GluN2B, and decreased GluA1 content in the synaptosome. In addition, we found that sustained MET signaling leads to intracortical excitatory connectivity changes; while the major inputs from L2/3 are decreased, L5 CSt neurons show increased inputs from L5 locations. It has been shown that critical period plasticity of cortical development involves extensive spine dynamics and structural remodeling (Majewska and Sur 2003), which enable proper selection of competing inputs driven by behavioral experience. In contrast to excitatory connectivity, cto-MET did not change inhibitory connectivity onto CSt neurons. Considering disrupted E/I balance is a posited circuit pathology in many neurodevelopmental disorders (Rubenstein and Merzenich 2003; Levitt et al. 2004; Lee et al. 2014; Sohal and Rubenstein 2019), our findings suggest potential disruption of E/I balance of specific intracortical circuits in mPFC. Collectively, these synaptic changes on L5 CSt neurons may lead to altered cortical outputs, as L5 projection neurons are involved in the top-down modulation of subcortical forebrain (e.g., striatum and amygdala) and brainstem (e.g., vagal) targets. L5 pyramidal neurons also receive inputs from all cortical layers and integrate multiple local and afferent pathways (Markram et al. 2015). L5 PFC neurons are among the cortical populations that normally express MET, appear to be vulnerable in ASD and other neurodevelopmental disorders (Willsey et al. 2013; Arion et al. 2015; Gao and Penzes 2015; Kalmbach et al. 2015; Gandhi and Lee 2020), and form circuits frequently implicated in generating complex cognitive, emotional regulatory, and social behaviors (Peca et al. 2011; Kim et al. 2016; Mei et al. 2016). In addition, since subsets of excitatory neurons express MET across cortical regions, it is conceivable that altered circuit outputs may be a common feature associated with mistimed MET signaling.

We have recently reported that in primary visual cortex, MET activates small GTPases that are coupled to molecular machinery operating at dendritic spines (Chen et al. 2020) and may account for the cell autonomous effects on spine morphogenesis observed in hippocampus CA1 neurons (Qiu et al. 2014). Here we found that cto-MET leads to persistent activation of Rac1 and cdc42 in PFC. Activation of Rac1 and Cdc42 is coupled to inhibitory phosphorylation of the actin filament depolymerizing protein cofilin (Arber et al. 1998; Carlisle et al. 2008; Calabrese et al. 2014). It is well established that Rho GTPase regulatory proteins control synapse development and structural plasticity (Luo 2002; Govek et al. 2005; Murakoshi et al. 2011; Tolia et al. 2011; Lai and Ip 2013). Cofilin is required for actin polymerization, which is critical for formation and enlargement of dendritic spines during neuronal activity (Penzes et al. 2011; Borovac et al. 2018) and AMPA receptor trafficking during

synaptic plasticity (Gu et al. 2010). Consistent with these findings, the results reported here suggest that dysregulated MET signaling that results in persistence may promote spine production and, through cofilin (Ser3) phosphorylation (Moriyama et al. 1996), inhibits spine actin dynamics that is required for activity-dependent spine pruning and refinement of connectivity (Arber et al. 1998; Gu et al. 2010; Calabrese et al. 2014). This hypothesis is supported by the present in vivo two-photon dendritic spine imaging data, which revealed increased spine formation and decreased elimination with sustained MET signaling. In comparison, terminating cto-MET at P35, which is beyond the normal period of pruning, leads to an increased rate of spine pruning. These data are consistent with our recent observation that turning off MET signaling after prolonged *Met* transgene expression opens a time window of heightened visual plasticity (Chen et al. 2020), well beyond the normal visual cortex critical period for monocular deprivation. Taken together, these data suggest that promotion of MET signaling during maturational growth phases of neurons, followed by termination, is an important regulatory sequence that may control balanced spine production and elimination, which is critical for normal synaptic connectivity.

A putative pathophysiology of autism is the disrupted timing synapse maturation, cortical circuit connectivity, and changes in activity-dependent plasticity that impinges on adult behavior (Aldinger et al. 2011; Berg and Geschwind 2012; Zoghbi and Bear 2012; Berger et al. 2013). Although MET is not causal for ASD, or implicated in ASD pathogenesis as revealed by genome wide association studies, MET-expressing neuronal circuits have been shown to modify mouse behavior, including social behavior, likely through altered interactions with transcription factors and synaptic signaling molecules (Campbell et al. 2006; Campbell et al. 2007; Xie et al. 2016). For example, 5-HT+ raphe neurons that express MET prenatally have been shown to modify social behavior (Okaty et al. 2015). We found that cto-MET does not affect basal locomotor activity and anxiety measures yet increases repetitive/stereotypical grooming, jumping, and marble-burying behaviors. Most remarkably, these mice show impaired sociability and reduced social novelty. The current work lends support to the emerging view that neurodevelopmental disorders such as ASD may be characterized in part by mistimed critical and sensitive periods of circuit development (LeBlanc and Fagiolini 2011; Berger et al. 2013; Krishnan et al. 2015).

Our results provide important new insights into an important developmental role for the temporal regulation of a pleiotropic signaling system, particularly as shown here in excitatory cortical neurons. We recently reported that young adult (2–3 months) *Met*<sup>CKO</sup> mice exhibited enhanced hippocampus plasticity, learning and memory, yet these mice showed early cognitive decline as they reach 10–12 months of age (Xia et al. 2021). Here, we further revealed the functional significance of the temporally delimited MET signaling by showing that extending MET signaling for two weeks after the abatement of endogenous MET leads to perpetuation of adult behavior. Thus, the impact of MET on the developing brain may be multifaceted, prolonged, and profound, which lends accumulating evidence that critical timing of molecular signaling events during development can have long-term effects on brain function (Ansorge et al. 2004; Thompson and Levitt 2010; Clement et al. 2012). The cellular, circuit, and behavior phenotypes described here inform how molecular regulatory mechanisms may result in specific network-level dysfunction that may not be causal for a specific

neurodevelopmental disorder but still have potent impact on the extent of phenotypic disturbances.

## Authors' contributions

Conceptualization, X.M., P.L., and S.Q.; Investigation, X.M., J.W., B.X., C.C., Y.C.; Formal Analysis, X.M., J.W., and S.Q.; Writing—Original draft, X.M. and S.Q.; Writing—Review and Editing, S.Q., P.L.; Funding Acquisition, S.Q. and P.L.; Supervision, D.F., P.L., and S.Q.

## Supplementary Material

Supplementary material is available at *Cerebral Cortex* online.

## Funding

National Institute of Health/National Institute of Mental Health grant (R01MH111619 to S.Q., R01MH067842 to P. L. and S.Q.); institution start-up fund from The University of Arizona (to S.Q.).

## Notes

The authors declare no competing interests.

## References

- Akimoto M, Baba A, Ikeda-Matsuo Y, Yamada MK, Itamura R, Nishiyama N, Ikegaya Y, Matsuki N. 2004. Hepatocyte growth factor as an enhancer of nmda currents and synaptic plasticity in the hippocampus. *Neuroscience*. 128:155–162.
- Aldinger KA, Lane CJ, Veenstra-VanderWeele J, Levitt P. 2015. Patterns of risk for multiple co-occurring medical conditions replicate across distinct cohorts of children with autism spectrum disorder. *Autism Res*. 8:771–781.
- Aldinger KA, Plummer JT, Qiu S, Levitt P. 2011. SnapShot: genetics of autism. *Neuron*. 72:418–418.e1.
- Aldinger KA, Timms AE, MacDonald JW, McNamara HK, Herstein JS, Bammler TK, Evgrafov OV, Knowles JA, Levitt P. 2020. Transcriptome data of temporal and cingulate cortex in the Rett syndrome brain. *Sci Data*. 7:192.
- Ansorge MS, Zhou M, Lira A, Hen R, Gingrich JA. 2004. Early-life blockade of the 5-HT transporter alters emotional behavior in adult mice. *Science*. 306:879–881.
- Arber S, Barbayannis FA, Hanser H, Schneider C, Stanyon CA, Bernard O, Caroni P. 1998. Regulation of actin dynamics through phosphorylation of cofilin by LIM-kinase. *Nature*. 393:805–809.
- Arion D, Corradi JP, Tang S, Datta D, Boothe F, He A, Cacace AM, Zaczek R, Albright CF, Tseng G, et al. 2015. Distinctive transcriptome alterations of prefrontal pyramidal neurons in schizophrenia and schizoaffective disorder. *Mol Psychiatry*. 20:1397–1405.
- Bagni C, Zukin RS. 2019. A synaptic perspective of fragile X syndrome and autism spectrum disorders. *Neuron*. 101:1070–1088.
- Berg JM, Geschwind DH. 2012. Autism genetics: searching for specificity and convergence. *Genome Biol*. 13:247.
- Berger JM, Rohn TT, Oxford JT. 2013. Autism as the early closure of a neuroplastic critical period normally seen in adolescence. *Biol Syst Open Access*. 2(3). doi: 10.4172/2329-6577.1000118.



- Borovac J, Bosch M, Okamoto K. 2018. Regulation of actin dynamics during structural plasticity of dendritic spines: signaling messengers and actin-binding proteins. *Mol Cell Neurosci*. 91:122–130.
- Bosch M, Castro J, Saneyoshi T, Matsuno H, Sur M, Hayashi Y. 2014. Structural and molecular remodeling of dendritic spine substructures during long-term potentiation. *Neuron*. 82:444–459.
- Calabrese B, Saffin JM, Halpain S. 2014. Activity-dependent dendritic spine shrinkage and growth involve downregulation of cofilin via distinct mechanisms. *PLoS One*. 9:e94787.
- Campbell DB, D'Oronzio R, Garbett K, Ebert PJ, Mirmics K, Levitt P, Persico AM. 2007. Disruption of cerebral cortex MET signaling in autism spectrum disorder. *Ann Neurol*. 62:243–250.
- Campbell DB, Sutcliffe JS, Ebert PJ, Milner R, Bravaccio C, Trillo S, Elia M, Schneider C, Melmed R, Sacco R, et al. 2006. A genetic variant that disrupts MET transcription is associated with autism. *Proc Natl Acad Sci U S A*. 103:16834–16839.
- Carlisle HJ, Manzerra P, Marcora E, Kennedy MB. 2008. SynGAP regulates steady-state and activity-dependent phosphorylation of cofilin. *J Neurosci*. 28:13673–13683.
- Chen K, Ma X, Nehme A, Wei J, Cui Y, Cui Y, Yao D, Wu J, Anderson T, Ferguson D, et al. 2020. Time-delimited signaling of MET receptor tyrosine kinase regulates cortical circuit development and critical period plasticity. *Mol Psychiatry*. doi: 10.1038/s41380-019-0635-6.
- Clement JP, Aceti M, Creson TK, Ozkan ED, Shi Y, Reish NJ, Almonte AG, Miller BH, Wiltgen BJ, Miller CA, et al. 2012. Pathogenic SYNGAP1 mutations impair cognitive development by disrupting maturation of dendritic spine synapses. *Cell*. 151:709–723.
- Dembrow N, Johnston D. 2014. Subcircuit-specific neuromodulation in the prefrontal cortex. *Front Neural Circuits*. 8:54.
- Dembrow NC, Zemelman BV, Johnston D. 2015. Temporal dynamics of L5 dendrites in medial prefrontal cortex regulate integration versus coincidence detection of afferent inputs. *J Neurosci*. 35:4501–4514.
- Dubbs A, Guevara J, Yuste R. 2016. Moco: fast motion correction for calcium imaging. *Front Neuroinform*. 10:6.
- Eagleson KL, Lane CJ, McFadyen-Ketchum L, Solak S, Wu HH, Levitt P. 2016. Distinct intracellular signaling mediates C-MET regulation of dendritic growth and synaptogenesis. *Dev Neurobiol*. 76:1160–1181.
- Eagleson KL, Milner TA, Xie Z, Levitt P. 2013. Synaptic and extrasynaptic location of the receptor tyrosine kinase met during postnatal development in the mouse neocortex and hippocampus. *J Comp Neurol*. 521:3241–3259.
- Eagleson KL, Xie Z, Levitt P. 2017. The pleiotropic MET receptor network: circuit development and the neural-medical Interface of autism. *Biol Psychiatry*. 81:424–433.
- Feng G, Mellor RH, Bernstein M, Keller-Peck C, Nguyen QT, Wallace M, Nerbonne JM, Lichtman JW, Sanes JR. 2000. Imaging neuronal subsets in transgenic mice expressing multiple spectral variants of GFP. *Neuron*. 28:41–51.
- Fox SE, Levitt P, Nelson CA 3rd. 2010. How the timing and quality of early experiences influence the development of brain architecture. *Child Dev*. 81:28–40.
- Fu M, Yu X, Lu J, Zuo Y. 2012. Repetitive motor learning induces coordinated formation of clustered dendritic spines in vivo. *Nature*. 483:92–95.
- Gandal MJ, Zhang P, Hadjimichael E, Walker RL, Chen C, Liu S, Won H, van Bakel H, Varghese M, Wang Y, et al. 2018. Transcriptome-wide isoform-level dysregulation in ASD, schizophrenia, and bipolar disorder. *Science*. 362:eaat8127.
- Gandhi T, Lee CC. 2020. Neural mechanisms underlying repetitive behaviors in rodent models of autism spectrum disorders. *Front Cell Neurosci*. 14:592710.
- Gao R, Penzes P. 2015. Common mechanisms of excitatory and inhibitory imbalance in schizophrenia and autism spectrum disorders. *Curr Mol Med*. 15:146–167.
- Genestine M, Caricati E, Fico A, Richelme S, Hassani H, Sunyach C, Lamballe F, Panzica GC, Pettmann B, Helmbacher F, et al. 2011. Enhanced neuronal met signalling levels in ALS mice delay disease onset. *Cell Death Dis*. 2:e130.
- Geschwind DH, Levitt P. 2007. Autism spectrum disorders: developmental disconnection syndromes. *Curr Opin Neurobiol*. 17:103–111.
- Gorski JA, Talley T, Qiu M, Puelles L, Rubenstein JL, Jones KR. 2002. Cortical excitatory neurons and glia, but not GABAergic neurons, are produced in the Emx1-expressing lineage. *J Neurosci*. 22:6309–6314.
- Gossen M, Bujard H. 1992. Tight control of gene expression in mammalian cells by tetracycline-responsive promoters. *Proc Natl Acad Sci U S A*. 89:5547–5551.
- Govek EE, Newey SE, Van Aelst L. 2005. The role of the rho GTPases in neuronal development. *Genes Dev*. 19:1–49.
- Grutzendler J, Kasthuri N, Gan WB. 2002. Long-term dendritic spine stability in the adult cortex. *Nature*. 420:812–816.
- Gu J, Lee CW, Fan Y, Komlos D, Tang X, Sun C, Yu K, Hartzell HC, Chen G, Bamberg JR, et al. 2010. ADF/cofilin-mediated actin dynamics regulate AMPA receptor trafficking during synaptic plasticity. *Nat Neurosci*. 13:1208–1215.
- Guang S, Pang N, Deng X, Yang L, He F, Wu L, Chen C, Yin F, Peng J. 2018. Synaptopathology involved in autism spectrum disorder. *Front Cell Neurosci*. 12:470.
- Gutierrez H, Dolcet X, Tolcos M, Davies A. 2004. HGF regulates the development of cortical pyramidal dendrites. *Development*. 131:3717–3726.
- Harlow EG, Till SM, Russell TA, Wijetunge LS, Kind P, Contractor A. 2010. Critical period plasticity is disrupted in the barrel cortex of FMR1 knockout mice. *Neuron*. 65:385–398.
- Hausott B, Kurnaz I, Gajovic S, Klimaschewski L. 2009. Signaling by neuronal tyrosine kinase receptors: relevance for development and regeneration. *Anat Rec (Hoboken)*. 292:1976–1985.
- Hensch TK. 2005. Critical period plasticity in local cortical circuits. *Nat Rev Neurosci*. 6:877–888.
- Hong SJ, Hyung B, Paquola C, Bernhardt BC. 2019. The superficial white matter in autism and its role in connectivity anomalies and symptom severity. *Cereb Cortex*. 29(10):4415–4425.
- Huang X, Stodieck SK, Goetze B, Cui L, Wong MH, Wenzel C, Hosang L, Dong Y, Lowel S, Schluter OM. 2015. Progressive maturation of silent synapses governs the duration of a critical period. *Proc Natl Acad Sci U S A*. 112:E3131–E3140.
- Jabaudon D. 2017. Fate and freedom in developing neocortical circuits. *Nat Commun*. 8:16042.
- Judson MC, Amaral DG, Levitt P. 2011. Conserved subcortical and divergent cortical expression of proteins encoded by orthologs of the autism risk gene MET. *Cereb Cortex*. 21:1613–1626.
- Judson MC, Bergman MY, Campbell DB, Eagleson KL, Levitt P. 2009. Dynamic gene and protein expression patterns of the autism-associated met receptor tyrosine kinase in the developing mouse forebrain. *J Comp Neurol*. 513:511–531.



- Kalmbach BE, Johnston D, Brager DH. 2015. Cell-type specific channelopathies in the prefrontal cortex of the *fmr1*-/- mouse model of fragile X syndrome. *eNeuro*. 2(6):e0114-15.
- Kast RJ, Levitt P. 2019. Precision in the development of neocortical architecture: from progenitors to cortical networks. *Prog Neurobiol*. 175:77-95.
- Kim H, Lim CS, Kaang BK. 2016. Neuronal mechanisms and circuits underlying repetitive behaviors in mouse models of autism spectrum disorder. *Behav Brain Funct*. 12:3.
- Krishnan K, Wang BS, Lu J, Wang L, Maffei A, Cang J, Huang ZJ. 2015. MeCP2 regulates the timing of critical period plasticity that shapes functional connectivity in primary visual cortex. *Proc Natl Acad Sci U S A*. 112:E4782-E4791.
- Lai KO, Ip NY. 2013. Structural plasticity of dendritic spines: the underlying mechanisms and its dysregulation in brain disorders. *Biochim Biophys Acta*. 1832:2257-2263.
- Lamballe F, Genestine M, Caruso N, Arce V, Richelme S, Helmbacher F, Maina F. 2011. Pool-specific regulation of motor neuron survival by neurotrophic support. *J Neurosci*. 31:11144-11158.
- Lambert N, Wermenbol V, Pichon B, Acosta S, van den Amele J, Perazzolo C, Messina D, Musumeci MF, Dessars B, De Leener A, et al. 2014. A familial heterozygous null mutation of MET in autism spectrum disorder. *Autism Res*. 7:617-622.
- LeBlanc JJ, Fagiolini M. 2011. Autism: a "critical period" disorder? *Neural Plast*. 2011:921680.
- Lee AT, Gee SM, Vogt D, Patel T, Rubenstein JL, Sohal VS. 2014. Pyramidal neurons in prefrontal cortex receive subtype-specific forms of excitation and inhibition. *Neuron*. 81:61-68.
- Lemmon MA, Schlessinger J. 2010. Cell signaling by receptor tyrosine kinases. *Cell*. 141:1117-1134.
- Levitt P, Campbell DB. 2009. The genetic and neurobiologic compass points toward common signaling dysfunctions in autism spectrum disorders. *J Clin Invest*. 119:747-754.
- Levitt P, Eagleson KL, Powell EM. 2004. Regulation of neocortical interneuron development and the implications for neurodevelopmental disorders. *Trends Neurosci*. 27:400-406.
- Li M, Santpere G, Imamura Kawasawa Y, Evgrafov OV, Gulden FO, Pochareddy S, Sunkin SM, Li Z, Shin Y, Zhu Y, et al. 2018. Integrative functional genomic analysis of human brain development and neuropsychiatric risks. *Science*. 362(6420):eaat7615.
- Liao D, Hessler NA, Malinow R. 1995. Activation of postsynaptically silent synapses during pairing-induced LTP in CA1 region of hippocampal slice. *Nature*. 375:400-404.
- Luo L. 2002. Actin cytoskeleton regulation in neuronal morphogenesis and structural plasticity. *Annu Rev Cell Dev Biol*. 18:601-635.
- Ma X, Chen K, Cui Y, Huang G, Nehme A, Zhang L, Li H, Wei J, Liong K, Liu Q, et al. 2020. Depletion of microglia in developing cortical circuits reveals its critical role in glutamatergic synapse development, functional connectivity, and critical period plasticity. *J Neurosci Res*. 98:1968-1986.
- Majewska A, Sur M. 2003. Motility of dendritic spines in visual cortex in vivo: changes during the critical period and effects of visual deprivation. *Proc Natl Acad Sci U S A*. 100:16024-16029.
- Markram H, Muller E, Ramaswamy S, Reimann MW, Abdellah M, Sanchez CA, Ailamaki A, Alonso-Nanclares L, Antille N, Arsever S, et al. 2015. Reconstruction and simulation of neocortical microcircuitry. *Cell*. 163:456-492.
- Maximo JO, Kana RK. 2019. Aberrant "deep connectivity" in autism: a cortico-subcortical functional connectivity magnetic resonance imaging study. *Autism Res*. 12:384-400.
- Mayford M, Bach ME, Huang YY, Wang L, Hawkins RD, Kandel ER. 1996. Control of memory formation through regulated expression of a CaMKII transgene. *Science*. 274:1678-1683.
- Mei Y, Monteiro P, Zhou Y, Kim JA, Gao X, Fu Z, Feng G. 2016. Adult restoration of Shank3 expression rescues selective autistic-like phenotypes. *Nature*. 530:481-484.
- Moriyama K, Iida K, Yahara I. 1996. Phosphorylation of Ser-3 of cofilin regulates its essential function on actin. *Genes Cells*. 1:73-86.
- Mukamel Z, Konopka G, Wexler E, Osborn GE, Dong H, Bergman MY, Levitt P, Geschwind DH. 2011. Regulation of MET by FOXP2, genes implicated in higher cognitive dysfunction and autism risk. *J Neurosci*. 31:11437-11442.
- Murakoshi H, Wang H, Yasuda R. 2011. Local, persistent activation of rho GTPases during plasticity of single dendritic spines. *Nature*. 472:100-104.
- Novak KD, Prevett D, Wang S, Gould TW, Oppenheim RW. 2000. Hepatocyte growth factor/scatter factor is a neurotrophic survival factor for lumbar but not for other somatic motoneurons in the chick embryo. *J Neurosci*. 20:326-337.
- Okaty BW, Freret ME, Rood BD, Brust RD, Hennessy ML, deBairos D, Kim JC, Cook MN, Dymecki SM. 2015. Multi-scale molecular deconstruction of the serotonin neuron system. *Neuron*. 88:774-791.
- Park H, Poo MM. 2013. Neurotrophin regulation of neural circuit development and function. *Nat Rev Neurosci*. 14:7-23.
- Parkhurst CN, Yang G, Ninan I, Savas JN, Yates JR 3rd, Lafaille JJ, Hempstead BL, Littman DR, Gan WB. 2013. Microglia promote learning-dependent synapse formation through brain-derived neurotrophic factor. *Cell*. 155:1596-1609.
- Peca J, Feliciano C, Ting JT, Wang W, Wells MF, Venkatraman TN, Lascola CD, Fu Z, Feng G. 2011. Shank3 mutant mice display autistic-like behaviours and striatal dysfunction. *Nature*. 472:437-442.
- Peng Y, Lu Z, Li G, Piechowicz M, Anderson MA, Uddin Y, Wu J, Qiu S. 2016. The autism associated MET receptor tyrosine kinase engages early neuronal growth mechanism and controls glutamatergic circuits development in the forebrain. *Mol Psychiatry*. 21:925-935.
- Penzes P, Cahill ME, Jones KA, VanLeeuwen JE, Woolfrey KM. 2011. Dendritic spine pathology in neuropsychiatric disorders. *Nat Neurosci*. 14:285-293.
- Plummer JT, Evgrafov OV, Bergman MY, Friez M, Haiman CA, Levitt P, Aldinger KA. 2013. Transcriptional regulation of the MET receptor tyrosine kinase gene by MeCP2 and sex-specific expression in autism and Rett syndrome. *Transl Psychiatry*. 3:e316.
- Pontrello CG, Sun MY, Lin A, Fiocco TA, DeFea KA, Ethell IM. 2012. Cofilin under control of beta-arrestin-2 in NMDA-dependent dendritic spine plasticity, long-term depression (LTD), and learning. *Proc Natl Acad Sci U S A*. 109:E442-E451.
- Qiu S, Anderson CT, Levitt P, Shepherd GM. 2011. Circuit-specific intracortical hyperconnectivity in mice with deletion of the autism-associated met receptor tyrosine kinase. *J Neurosci*. 31:5855-5864.
- Qiu S, Lu Z, Levitt P. 2014. MET receptor tyrosine kinase controls dendritic complexity, spine morphogenesis, and glutamatergic synapse maturation in the hippocampus. *J Neurosci*. 34:16166-16179.
- Ramaswami G, Won H, Gandal MJ, Haney J, Wang JC, Wong CCY, Sun W, Prabhakar S, Mill J, Geschwind DH. 2020. Integrative

- genomics identifies a convergent molecular subtype that links epigenomic with transcriptomic differences in autism. *Nat Commun.* 11:4873.
- Reh RK, Dias BG, Nelson CA 3rd, Kaufer D, Werker JF, Kolb B, Levine JD, Hensch TK. 2020. Critical period regulation across multiple timescales. *Proc Natl Acad Sci U S A.* 117:23242–23251.
- Rein B, Ma K, Yan Z. 2020. A standardized social preference protocol for measuring social deficits in mouse models of autism. *Nat Protoc.* 15:3464–3477.
- Rubenstein JL, Merzenich MM. 2003. Model of autism: increased ratio of excitation/inhibition in key neural systems. *Genes Brain Behav.* 2:255–267.
- Rudie JD, Hernandez LM, Brown JA, Beck-Pancer D, Colich NL, Gorrindo P, Thompson PM, Geschwind DH, Bookheimer SY, Levitt P, et al. 2012. Autism-associated promoter variant in MET impacts functional and structural brain networks. *Neuron.* 75:904–915.
- Sarmiere PD, Bamberg JR. 2004. Regulation of the neuronal actin cytoskeleton by ADF/cofilin. *J Neurobiol.* 58:103–117.
- Schafer DP, Stevens B. 2013. Phagocytic glial cells: sculpting synaptic circuits in the developing nervous system. *Curr Opin Neurobiol.* 23:1034–1040.
- Searles Quick VB, Wang B, State MW. 2021. Leveraging large genomic datasets to illuminate the pathobiology of autism spectrum disorders. *Neuropsychopharmacology.* 46:55–69.
- Shepherd GM, Svoboda K. 2005. Laminar and columnar organization of ascending excitatory projections to layer 2/3 pyramidal neurons in rat barrel cortex. *J Neurosci.* 25:5670–5679.
- Sholl DA. 1953. Dendritic organization in the neurons of the visual and motor cortices of the cat. *J Anat.* 87:387–406.
- Silverman JL, Yang M, Lord C, Crawley JN. 2010. Behavioural phenotyping assays for mouse models of autism. *Nat Rev Neurosci.* 11:490–502.
- Sohal VS, Rubenstein JLR. 2019. Excitation-inhibition balance as a framework for investigating mechanisms in neuropsychiatric disorders. *Mol Psychiatry.* 24:1248–1257.
- Stephany CE, Chan LL, Parivash SN, Dorton HM, Piechowicz M, Qiu S, McGee AW. 2014. Plasticity of binocularity and visual acuity are differentially limited by nogo receptor. *J Neurosci.* 34:11631–11640.
- Sullivan PF, Geschwind DH. 2019. Defining the genetic, genomic, cellular, and diagnostic architectures of psychiatric disorders. *Cell.* 177:162–183.
- Suter BA, O'Connor T, Iyer V, Petreanu LT, Hooks BM, Kiritani T, Svoboda K, Shepherd GM. 2010. Ephus: multipurpose data acquisition software for neuroscience experiments. *Front Neural Circuits.* 4:100.
- Tau GZ, Peterson BS. 2010. Normal development of brain circuits. *Neuropsychopharmacology.* 35:147–168.
- Thompson BL, Levitt P. 2010. The clinical-basic interface in defining pathogenesis in disorders of neurodevelopmental origin. *Neuron.* 67:702–712.
- Tolias KF, Duman JG, Um K. 2011. Control of synapse development and plasticity by rho GTPase regulatory proteins. *Prog Neurobiol.* 94:133–148.
- Willsey AJ, Sanders SJ, Li M, Dong S, Tebbenkamp AT, Muhle RA, Reilly SK, Lin L, Fertuzinhos S, Miller JA, et al. 2013. Coexpression networks implicate human midfetal deep cortical projection neurons in the pathogenesis of autism. *Cell.* 155:997–1007.
- Wittkowski KM, Sonakya V, Bigio B, Tonn MK, Shic F, Ascano M, Nasca C, Gold-Von Simson G. 2014. A novel computational biostatistics approach implies impaired dephosphorylation of growth factor receptors as associated with severity of autism. *Transl Psychiatry.* 4:e354.
- Won H, Lee HR, Gee HY, Mah W, Kim JI, Lee J, Ha S, Chung C, Jung ES, Cho YS, et al. 2012. Autistic-like social behaviour in Shank2-mutant mice improved by restoring NMDA receptor function. *Nature.* 486:261–265.
- Xia B, Wei J, Ma X, Nehme A, Liong K, Cui Y, Chen C, Gallitano A, Ferguson D, Qiu S. 2021. Conditional knockout of MET receptor tyrosine kinase in cortical excitatory neurons leads to enhanced learning and memory in young adult mice but early cognitive decline in older adult mice. *Neurobiol Learn Mem.* 179:107397.
- Xie Z, Eagleson KL, Wu HH, Levitt P. 2016. Hepatocyte growth factor modulates MET receptor tyrosine kinase and  $\beta$ -catenin functional interactions to enhance synapse formation. *eNeuro.* 3:ENEURO.0074–ENEURO16.2016.
- Yang G, Pan F, Parkhurst CN, Grutzendler J, Gan WB. 2010. Thinned-skull cranial window technique for long-term imaging of the cortex in live mice. *Nat Protoc.* 5:201–208.
- Yang N, Higuchi O, Ohashi K, Nagata K, Wada A, Kangawa K, Nishida E, Mizuno K. 1998. Cofilin phosphorylation by LIM-kinase 1 and its role in Rac-mediated actin reorganization. *Nature.* 393:809–812.
- Yu X, Zuo Y. 2014. Two-photon in vivo imaging of dendritic spines in the mouse cortex using a thinned-skull preparation. *J Vis Exp.* (87):e51520. <https://doi.org/10.3791/51520>.
- Zhan Y, Paolicelli RC, Sforazzini F, Weinhard L, Bolasco G, Pagani F, Vyssotski AL, Bifone A, Gozzi A, Ragozzino D, et al. 2014. Deficient neuron-microglia signaling results in impaired functional brain connectivity and social behavior. *Nat Neurosci.* 17:400–406.
- Zoghbi HY, Bear MF. 2012. Synaptic dysfunction in neurodevelopmental disorders associated with autism and intellectual disabilities. *Cold Spring Harb Perspect Biol.* 4:a009886.